

On universal features of the turbulent cascade in terms of non-equilibrium thermodynamics

Nico Reinke^{1,2†}, Andre Fuchs^{1,2}, Daniel Nickelsen^{1,3,4}, and Joachim Peinke^{1,2}

¹Institute of Physics, University of Oldenburg

²ForWind, University of Oldenburg, Carl-von-Ossietzky-Str. 9-11, 26129 Oldenburg, Germany

³National Institute for Theoretical Physics (NITheP), Stellenbosch 7600, South Africa

⁴Institute of Theoretical Physics, University of Stellenbosch, South Africa

(Received xx; revised xx; accepted xx)

Features of the turbulent cascade are investigated for various datasets from three different turbulent flows, namely free jets as well as wake flows of a regular grid and a cylinder. The analysis is focused on the question as to whether fully developed turbulent flows show universal small scale features. Two approaches are used to answer this question. Firstly, 2-point statistics, namely structure functions of longitudinal velocity increments and secondly, joint multi-scale statistics of these velocity increments are analysed. The joint multi-scale characterisation encompasses the whole cascade in one joint probability density function. On the basis of the datasets, evidence of the Markov property for the turbulent cascade is shown, which corresponds to a three point closure that reduces the joint multi-scale statistics to simple conditional probability density functions (cPDF). The cPDF are described by the Fokker-Planck equation in scale and its Kramers-Moyal coefficients (KMCs). KMCs are obtained by a self-consistent optimisation procedure from the measured data and result in a Fokker-Planck equation for each dataset. The knowledge of these stochastic cascade equations enables to make use of the concepts of non-equilibrium thermodynamics and thus to determine the entropy production along individual cascade trajectories. In addition to this new concept, it is shown that the local entropy production is nearly perfectly balanced for all datasets by the integral fluctuation theorem (IFT). Thus the validity of the IFT can be taken as a new law of the turbulent cascade and at the same time independently confirms that the physics of the turbulent cascade is a memoryless Markov process in scale. IFT is taken as a new tool to prove the optimal functional form of the Fokker-Planck equations and subsequently to investigate the question of universality of small scale turbulence in the datasets. The results of our analysis show that the turbulent cascade contains universal and non-universal features. We identify small scale intermittency as a universality breaking feature. We conclude that specific turbulent flows have their own particular multi-scale cascade, with other words their own stochastic fingerprint.

1. Introduction

A general description of turbulent flows remains one of the most challenging unsolved scientific problems, e.g. Nelkin (1992); Clay (2000). Of particular importance is the simplified problem of homogeneous isotropic turbulence (HIT). HIT is not only often

† Email address for correspondence: peinke@uni-oldenburg.de

the starting point for fundamental studies, but also important for applications like CFD-modelling, where the features of small scale turbulence are essential for simplifications, e.g. Pope (2000).

The idea and the profound understanding of turbulence as a cascade process, cf. Frisch (2001), plays an important role for such simplifications. The turbulent cascade can be understood as the evolution of turbulent structures with varying spatial size given by a scale r . The evolution can be divided into 3 stages. Firstly, turbulence is initiated at large scales, characterised by the integral length scale L . Secondly, the generated large scale structures decay throughout the cascade process. It is expected that this decay process is self-similar until, thirdly, it ends at a micro scale, where the viscosity of the fluid starts to significantly affect the decay. The range of non-dissipative scales is called the inertial range and it is this range where we have performed our analysis.

One important question for the understanding of the turbulent cascade is how turbulent structures evolve within the inertial range. Strongly related to this issue is the question as to whether turbulent structures evolve in a universal way, or whether the evolution depends on the generation process and its specific large scale features. With other words, how long do large turbulent structures have a significant impact to small scale features? This central question is frequently discussed in literature since the contributions of Kolmogorov and Landau, cf. Frisch (2001, pp. 93-98) and it is essential for the concept of universal small scale turbulence.

The overwhelming majority of studies investigate turbulence by statistics of increments u_r like structure functions $S^\kappa(u_r)$. For HIT, scaling features of structure functions are commonly assumed as a function of scale r , characterised by a scaling exponent ξ_κ , cf. Kolmogorov (1941, 1962); Frisch (2001); Davidson (2004); Pope (2000). Universality is assumed to be found in the scaling exponents ξ_κ , whereas pre-factors may change with different flow conditions, cf. Kolmogorov (1962). Within this context, works on finite size effects, Dubrulle (2000), or the understanding of multi-scale excited turbulent flows and its structures, e.g. Kuczaj *et al.* (2006); Hurst & Vassilicos (2007); Valente & Vassilicos (2012); Nagata *et al.* (2013), are of particular interest.

Note that the structure function analysis can be expressed equivalently by probability density functions $p(u_r)$ (PDF). From a statistical point of view, structure functions as well as increment PDFs are two point quantities, i.e. the relation of velocities at two points separated by a selected distance, the scale r , is investigated.

It was shown, e.g. in Renner *et al.* (2002b), that 2-point statistics do not completely characterise the features of small scale turbulence. A general multi-scale characterisation of the turbulent cascade can be expressed by the joint PDF $p(u_r; u_{r+\Delta}; \dots; u_{r+N\Delta})$ at N scales r . Reviews on the stochastic processes in general and in the context of turbulence can be found in Friedrich & Peinke (2009); Friedrich *et al.* (2011). Since velocity increment series show the Markov property, the joint PDF can equally be expressed by a chain of conditional PDFs $p(u_r|u_{r+\Delta})$, cf. Friedrich & Peinke (1997a); Renner *et al.* (2001); Tutkun & Mydlarski (2004). Note that this Markov property corresponds to a 2-scale or 3-point closure of the generalised multi-scale joint probability. Furthermore, an evolution of this transition probability $p(u_r|u_{r+\Delta})$ along the scale can be described by the Fokker-Planck equation, where only the first two Kramers-Moyal coefficients $D^{(1)}(u_r)$ and $D^{(2)}(u_r)$ govern the equation. Thus, these two Kramers-Moyal coefficients describe the stochastic features of the turbulent cascade along the inertial range. Thereby, different cascades, measured in different turbulent flows, can be set into a quantitative comparison with these two coefficients. Note, similar to this approach, other approaches contain equivalent joint multi-scale information of the turbulent cascade, cf. Lundgren (1967); Monin (1967); L'vov & Procaccia (1996); Davoudi & Tabar (2000); Monin *et al.* (2007).

In the discussion of cascade models for multifractal features of turbulence, relations similar to the Markov condition were implicitly discussed. Quantities and kernel functions relating different scales were used Novikov (1994); Castaing & Dubrulle (1995); She & Waymire (1995); Arneodo *et al.* (1997), sometimes with the concept of infinitely divisible distributions. These scale relating features can be considered as Chapman-Kolmogorov conditions. The indicated works may therefore be considered as first works in the direction of stochastic cascade processes, however, energy and energy related quantities of the cascades were considered and not the velocity increment itself. Some of these works already put proper scaling behaviour and flow independent universalities for the increment statistics into question.

A different approach using the Langevin equation for the stochastic description of the cascade was presented in Marcq & Naert (2001). Based on the Langevin equation, the authors reconstructed the noise along the cascade and showed that it is uncorrelated. In their analysis the connection to structure functions were investigated and it was concluded that the odd order structure function could be grasped by the stochastic approach only qualitatively. Furthermore, they posed the question as to what extend the stochastic analysis of the cascade depends on the nature of the turbulent flow, a point which will be discussed in this paper in detail.

Renner *et al.* (2001) applied such a multi-scale analysis to turbulent data taken in a free jet experiment and the Kramers-Moyal coefficients were related to structure functions. In Renner *et al.* (2002b) it is shown that the multi-scale statistics of free jet generated turbulent cascades change with Taylor-Reynolds number (Re_λ), and the issue of universal features of small scale turbulence was discussed. In Siefert & Peinke (2004, 2006) the common stochastic process of longitudinal and transversal velocity increments were investigated and the relation to the Karman equation was shown. A similar work addressed the statistics of passive scalars, c.f. Tutkun & Mydlarski (2004); Melius *et al.* (2014), where the features of a turbulent flow was analysed in terms of Kramers-Moyal coefficients from which the stochastic flow features could be reconstructed.

Based on multi-scale statistics, Stresing *et al.* (2010) found that fractal grid generated turbulence exhibits different scaling features and multi-scale statistics than *commonly* generated flows (cylinder wake and free jet), defining a novel class of turbulence. The work of Stresing & Peinke (2010); Keylock *et al.* (2015) gives first indications that the turbulent cascade and its Kramers-Moyal coefficients depend on the turbulence generation mechanism. This dependence on turbulence generation contrasts with the universal features found on the basis of 2-point statistics involving structure functions and its scaling exponents. Therefore, we revive this analysis with 2-point and joint multi-scale statistics and study the question of universality in more detail and in a more general as well as more systematic way.

Although the joint multi-scale statistics will deliver more details of the complex structure of turbulence, an issue remains with the accuracy in determining the Kramers-Moyal coefficients, since one has to bridge the Einstein-Markov length for their estimation, cf. R. Friedrich & Peinke (1998); Renner *et al.* (2001); Lück *et al.* (2006). † Two ways to overcome this technical difficulty have been worked out and applied in this investigation. Firstly, the Kramers-Moyal coefficients are estimated by an optimisation procedure. Thus, Kramers-Moyal coefficients matches best to the experimental found data, namely $p(u_r|u_{r+\Delta})$, cf. Nawroth *et al.* (2007); Kleinhans *et al.* (2005). Secondly, an

† Note that a general feature of continuous stochastic processes is that it interpolates the real process, such as the deterministic motion of a particle in a diffusion process, or the dissipative structures in turbulent flows considered here.

independent way to assess the adequacy of the Kramers-Moyal coefficients is based on an integral fluctuation theorem (IFT), cf. Seifert (2005). The IFT is a generalisation of the second law to the non-equilibrium thermodynamics of small systems. Recently, the formal applicability of the IFT to turbulent cascade processes has been demonstrated by Nickelsen & Engel (2013) for a free jet flow.

In our paper, we confirm the applicability of the IFT for a total number of 61 different turbulent flows and explore its implications. As the IFT is based on the knowledge of the underlying stochastic process, we report in this paper in detail the advances which have been worked out for the reconstruction of the Fokker-Planck equation from given data. Moreover, we use the IFT as a criterion for the adequacy of the estimated stochastic process equations. It is the first time, that the IFT is verified and utilised for such a comprehensive dataset comprising various types of turbulent flows at a wide range of Reynolds numbers, which is our first main result.

A particular benefit of including the IFT into the estimation procedure is the pronounced sensitivity of the IFT with regard to the proper modelling of small scale intermittency. Thus, the IFT can be taken as an independent evidence for the Markov property of the turbulent cascade. Utilising this sensitivity, we are further able to pin down the minimal functional form of the first two Kramers-Moyal coefficients and still respect the features of small scale turbulence, which is our second main result[†].

This new approach enables to draw the analogy to non-equilibrium thermodynamic processes, sheds light on the essential mechanisms of the cascade process and identifies an energetic term u^2 as the source of intermittent small scale fluctuations.

Finally, the combination of the optimisation procedure and the IFT allows us a profound comparison of stochastic features of the different turbulent flows. We conclude that, within the inertial range and on small scales, universal and non-universal contributions are present. In particular, intermittent features of the cascade can be identified as universality breaking, which is our third main result.

The basis of our analysis forms the longitudinal velocity increment component of 61 datasets, mostly measured by hot-wires, where the turbulence was generated by regular grid, cylinder and free jet, and cover a Taylor-Reynolds number range of $28 \leq Re_\lambda \leq 996$. The entire data was always used, no single dataset has been sorted out for reasons of clarity.

This paper is organised as follows: In section 2 we give more information about the analysed datasets, section 3 details the used methods regarding structure functions, the IFT and the multi-scale analysis. In section 4 the results are presented, followed by a discussion against the background of universality and the cascade process. Section 5 concludes the paper.

2. Data basis

The data basis used in this study consists of 61 single datasets, which correspond to seven subgroups, namely i) regular grid generated turbulence, with $28 \leq Re_\lambda \leq 153$, cf. Lück *et al.* (2006), ii) cylinder wake turbulence at the relative distance $\frac{x}{D}=40$ with $261 \leq Re_\lambda \leq 894$, cf. Lück *et al.* (2006), iii) cylinder wake turbulence at various positions $\frac{x}{D}=50, 60, 70, 80, 90$ and 100 with $Re_\lambda \approx 261$, cf. Lück *et al.* (2006), iv) free jet generated turbulence in helium at $\frac{x}{D}=40$ with $208 \leq Re_\lambda \leq 996$, cf. Chanal *et al.* (2000), v) free jet turbulence in air at $\frac{x}{D}=40$, vi) free jet turbulence in air at $\frac{x}{D}=60$ and vii) free jet

[†] See also a preliminary use of this procedure in a data analysis of turbulence generated by a fractal grid, Reinke *et al.* (2016).

Dataset	Re_λ [-]	L [mm]	λ [mm]	l_{EM} [mm]	Θ [mm]	σ_v [m/s]	σ_Θ [m/s]
i) grid	153	25.0	2.61	5.22	6.57	0.845	0.637
iii) cylinder	894	25.2	3.35	6.70	9.78	3.94	2.40
iv) jet (2)	996	1.95	0.186	0.372	0.464	0.183	0.119
vii) jet (1)	166	62.5	5.84	11.7	15.7	0.382	0.278

TABLE 1. Exemplary datasets and their characteristics.

turbulence in air at $\frac{x}{D}=80$. The free jet data in air cover the Taylor Reynolds number range of $166 \leq Re_\lambda \leq 865$. x denotes in all cases the downstream position, D the cylinder diameter or the jet nozzle diameter.

The subgroups i), ii), v)-vii) are measured with a single hot-wire probe and contain longitudinal velocity component measurements. The subgroup iii) is measured with a X-wire probe, therefore these data contain the longitudinal and one transversal velocity component, which is not analysed here. The subgroup iv) is measured with a special micro structured hot-point probe, cf. Chanal *et al.* (2000). This measurement technique is similar to a single hot-wire probe.

In the following, results of the single subgroups are indicated by the following markers and notations in legends: i) open squares, *Grids*; ii) open circles, *Cylinders*; iii) solid circles, greyscale indicates $\frac{x}{D}$, the darker the larger $\frac{x}{D}$, *Cylinders (x/D)*; iv) open triangles, *Jets He*; v) solid triangles, *Jets 40D*; vi) open triangles, *Jets 60D* and vii) solid triangles, *Jets 80D*. Open and solid triangles are differently oriented in order to improve their distinctness.

Four exemplary datasets are used to highlight the results of our analysis. These datasets are chosen either to be comparable in terms of Taylor-Reynolds number Re_λ (namely 153 and 166 or 894 and 996) or to be comparable in the kind of turbulence generation. Characteristic quantities of these datasets are summarised in table 1. The listed quantities are, longitudinal integral length L , Taylor micro scale length λ , a newly defined Kolmogorov length scale Θ , standard deviation of the velocity σ_v and a newly defined standard deviation σ_Θ for normalisation.

To estimate λ , the procedure proposed by Aronson & Löfdahl (1993) is used, in good agreement with the findings in Lück *et al.* (2006) and Renner *et al.* (2001). The integral length L is estimated by integrating the autocorrelation function, cf. Batchelor (1953). In case of a non-monotonous decrease of the autocorrelation function (until first zero crossing) the autocorrelation function is extrapolated by an exponential function, cf. Reinke *et al.* (2014). More information regarding this procedure can be found in appendix A1. Results of L match with findings in Lück *et al.* (2006) and Renner *et al.* (2001). Note also that the ratio $\frac{L}{\lambda}$ as a function of Re_λ is shown in appendix A1, which demonstrates the consistency of the used datasets. Θ and σ_Θ are defined in section 3.

3. Methods of analysis

This section discusses the methods we use to analyse our data. First the classical method based on structure functions is briefly summarised, before we discuss in some more detail the method used to achieve a multi-scale analysis by means of stochastic processes. In particular, the procedure to obtain from the data a best estimate for a cascade Fokker-Planck equation is discussed. Finally, we show how the estimated cascade

equation can be used to determine the entropies for which the integral fluctuation theorem is a rigorous law.

3.1. Classical analysis

At first, datasets of velocity time series are transferred to spatial velocity series by the use of Taylor's hypothesis,

$$v(dx) \approx v(-\langle v(t) \rangle dt), \quad (3.1)$$

where v denotes the velocity component in the main flow direction, x is the spatial component in the main flow direction, t is time and $\langle \dots \rangle$ denotes the expectation value. The minus sign in eq. (3.1) aligns the orientation of the x -axis with the flow direction. Taylor's hypothesis of frozen turbulence is commonly known as a good approximation for small velocity fluctuations $\frac{v'}{\langle v \rangle} \ll 1$, cf. Taylor (1938), or small turbulence intensities, i.e. smaller than 10-20%, cf. Murzyn & B elorgey (2005). This limit is fulfilled for almost all datasets. Further discussion of the validity can be found e.g. in Lin (1950); Lumley (1965); Pinton, J. F. & Labb e, R. (1994); Tong & Warhaft (1995); Gledzer (1997).

A standard quantity to analyse the scaling of turbulence is the velocity increment

$$u_r^* := v(x+r) - v(x), \quad (3.2)$$

which is the difference of velocities at two points separated by the distance r , therefore its statistics is referred to as 1-scale statistics or, respectively, 2-point statistics on scale r . A common quantity for the analysis of turbulence is the so-called structure function of order κ ,

$$S^\kappa(r) = \langle (u_r^*)^\kappa \rangle. \quad (3.3)$$

Within the inertial range, it is commonly proposed that for homogeneous isotropic turbulence, structure functions scale according to a power law (Kolmogorov 1941)

$$S^\kappa(r) \propto r^{\xi_\kappa}. \quad (3.4)$$

Kolmogorov (1962) proposed a refined approach for the structure function exponent (K62),

$$\xi_\kappa = \frac{\kappa}{3} - \frac{\mu}{18} \kappa(\kappa - 3), \quad (3.5)$$

with the experimentally measured intermittency factor $\mu \approx 0.26$, e.g. Arneodo *et al.* (1996). While Kolmogorov proposed the scaling exponents ξ_κ to be constant in r , a local scaling exponent $\xi_\kappa(r)$ can be calculated from experimental data by the log-log-derivative of structure functions. Here, the central difference quotient is used,

$$\xi_\kappa(r) = \lim_{\delta r \rightarrow 0} \frac{\ln(\langle (u_{r+\delta r}^*)^\kappa \rangle) - \ln(\langle (u_{r-\delta r}^*)^\kappa \rangle)}{\ln(r + \delta r) - \ln(r - \delta r)}. \quad (3.6)$$

Experimental results (as shown below) show that the range of constant scaling is rather small or even infinitesimal in case of finite Taylor based Reynolds numbers ($Re_\lambda \leq 1000$). This motivates to define a specific scale Θ at $\xi_2(\Theta) = 0.696$, where the scaling proposed by Kolmogorov is located. Correspondingly, a standard deviation $\sigma_\Theta = \sqrt{\langle (u_{r=\Theta}^*)^2 \rangle}$ is defined. Here, we call Θ *Kolmogorov length scale* (of second order).

For the comparison of the statistics of u_r^* , it is necessary that velocity increments are normalised in a proper way. On the one side, we follow the way proposed by Renner *et al.* (2001), where a norm based on second order structure function is used, and on the other side, we are inspired by the work of Mydlarski & Warhaft (1996), where features of the inertial range are investigated. To account for both, we select σ_Θ for the purpose

of normalisation,

$$u_r := \frac{u_r^*}{\sigma_\Theta}. \quad (3.7)$$

The benefit of this normalisation becomes more clear below and it should be noted that this normalisation can be applied without loss of generality in scaling features. This fact can easily be shown, for instance with eqs. (3.3) and (3.4), where a multiplication with an arbitrary factor does not change the scaling exponent.

3.2. Joint multi-scale analysis

Structure functions can be expressed in terms of unconditional probability density functions $p(u_r)$,

$$S^\kappa(r) = \int_{-\infty}^{+\infty} u_r^\kappa p(u_r) du_r. \quad (3.8)$$

Thus, the information given by all structure functions is equivalent to the information of $p(u_r)$ at r , cf. Frisch (2001). Approaches using eq. (3.8) consider the statistical features for each scale separately. As the turbulent cascade is a chain of events on different scales, a more appropriate approach sets the statistics of scales in relation to each other. A N -scale joint PDF $p(u_r; u_{r+\Delta}; u_{r+2\Delta}; \dots; u_{r+N\Delta})$ captures the entire multi-scale characteristics of the turbulent cascade including its relations over different scales, cf. Friedrich & Peinke (1997a).

Earlier studies show that both the turbulent cascade process and its increment series have the Markov property, e.g. Friedrich & Peinke (1997a); Renner *et al.* (2001, 2002b); Tutkun & Mydlarski (2004); Lück *et al.* (2006). Thus, general joint PDFs can be expressed by conditional PDFs,

$$\begin{aligned} p(u_r; u_{r+\Delta}; \dots; u_{r+N\Delta}) &= p(u_r|u_{r+\Delta})p(u_{r+\Delta}|u_{r+2\Delta}) \times \dots \\ &\times p(u_{r+(N-1)\Delta}|u_{r+N\Delta})p(u_{r+N\Delta}). \end{aligned} \quad (3.9)$$

Motivated by the cascade picture, our notation here implies that an increment u_r is conditioned on an increment on a larger scale $u_{r+\Delta}$.

The Markov property is commonly only valid for finite step sizes, in particular when the deterministic microscopic or smallest scale dynamics is coarse-grained to a stochastic dynamics, cf. Einstein (1905). In the case of the turbulent cascade it is valid for $\Delta \geq l_{EM}$, where l_{EM} is the Einstein-Markov coherence length and it is $l_{EM} \propto \lambda$, cf. Lück *et al.* (2006); Stresing *et al.* (2012). Unless stated otherwise, we take the step width in the cascade as $\Delta = l_{EM} = 2\lambda$. Details of the determination of the Einstein-Markov coherence length are given in appendix A2. Thus, the stochastic process at scale r is determined by the conditional PDF $p(u_r|u_{r+l_{EM}})$ and the entire cascade with its interscale relations can be described by $p(u_r|u_{r+l_{EM}})$ as function of r .

Starting from an initial distribution, e.g. at the integral length scale, $p(u_L)$, or any other starting scale r' , the evolution of $p(u_r|u_L)$ can be described by the Fokker-Planck equation (also known as Kolmogorov equation), cf. Friedrich & Peinke (1997a,b); Renner *et al.* (2001),

$$\begin{aligned} -\frac{\partial}{\partial r} p(u_r|u_{r'}) &= -\frac{\partial}{\partial u_r} \left[D^{(1)}(u_r) p(u_r|u_{r'}) \right] \\ &+ \frac{\partial^2}{\partial u_r^2} \left[D^{(2)}(u_r) p(u_r|u_{r'}) \right]. \end{aligned} \quad (3.10)$$

Thereby, any $p(u_r|u_{r'})$ with $r < r'$ can be obtained. The functions $D^{(1)}(u_r)$ and $D^{(2)}(u_r)$

govern the Fokker-Planck equation and are known as drift and diffusion functions or, more generally, first and second Kramers-Moyal coefficients. The Fokker-Planck equation is a truncated Kramers-Moyal expansion, cf. Risken (1984), where only the first two terms are considered. Due to the fact that the first two terms of the Kramers-Moyal expansion strongly dominate the expansion, cf. Renner *et al.* (2001); Tutkun & Mydlarski (2004), the description of the evolution of the conditional PDFs in scale by the Fokker-Planck equation is justified. This dominance can be related to Pawula's theorem, which further corroborates the use of the Fokker-Planck equation, cf. Risken (1984).

The Fokker-Planck approach can be related to structure functions by partial integration of eq. (3.10), e.g. Friedrich *et al.* (1997); Renner *et al.* (2001),

$$-r \frac{\partial}{\partial r} S^\kappa(r) = r\kappa \langle u_r^{(\kappa-1)} D^{(1)}(u_r) \rangle + r\kappa(\kappa-1) \langle u_r^{(\kappa-2)} D^{(2)}(u_r) \rangle. \quad (3.11)$$

It is easily seen that this set of equations for S^κ becomes unclosed if the drift and diffusion functions have higher order contributions in u_r ($D^{(1)}$ higher than linear, $D^{(2)}$ higher than quadratic).

Besides the Fokker-Planck equation, the two coefficients $D^{(1)}(u_r)$ and $D^{(2)}(u_r)$ define the equivalent Langevin equation (cf. Risken (1984)). The Langevin equation describes the evolution of increments u_r in r as trajectories $u(\cdot)$. The trajectory level illustrates our novel way of investigating turbulence by considering cascade trajectories of increments $u_L \rightarrow u_r$.

3.3. Estimation of Kramers-Moyal coefficients

Next, technical aspects are discussed on how to estimate the best Fokker-Planck equation. Kramers-Moyal coefficients can be estimated from given data by conditional moments,

$$M^{(\kappa)}(u_{r'}, \delta) = \int_{-\infty}^{+\infty} (\tilde{u}_r - u_{r'})^\kappa p(\tilde{u}_r | u_{r'}) d\tilde{u}_r, \quad (3.12)$$

$$= \langle [\tilde{u}_r - u_{r'}]^\kappa \rangle_{u_{r'}} \quad (3.13)$$

$$D^{(\kappa)}(u_{r'}) = \lim_{\delta \rightarrow 0} \frac{1}{\kappa! \delta} M^{(\kappa)}(u_{r'}, \delta), \quad (3.14)$$

where κ is the order of the coefficient, cf. Risken (1984) and $\delta = r' - r$. A common method to estimate $\lim_{\delta \rightarrow 0}$ in eq. (3.14) is an extrapolation. The evolution of moments $M^{(\kappa)}(u_r, \delta)$ between $\delta = l_{EM}$ and $\delta = 2l_{EM}$ is linearly extrapolated to $\delta = 0$ and the intersection with the ordinate axis estimates the limit. Kramers-Moyal coefficients deduced by this approach lead to a rather imprecise description of the turbulent cascade. Further improvements are possible with the use of higher order corrections, see Risken (1984) and discussions of this issue in Gottschall & Peinke (2008); Renner (2002), and Honisch & Friedrich (2011). Nevertheless, the limit approximation leads to uncertainties and still leaves room for improvements for their absolute values, whereas the functional form of Kramers-Moyal coefficients are commonly well estimated.

To determine the Kramers-Moyal coefficients, an optimisation procedure is used to minimise possible uncertainties, which was proposed in Nawroth *et al.* (2007); Kleinhans *et al.* (2005). Four steps are necessary for this optimisation: i) parametrisation of Kramers-Moyal coefficients, ii) calculation of $p(u_r; u_{r+l_{EM}})$, iii) estimating the difference between calculated distribution $p(u_r; u_{r+l_{EM}})$ and measured joint PDF and iv) an iterative optimisation procedure that finds best fitting Kramers-Moyal coefficients, ensuring a minimal distance between the distributions.

We discuss the four steps in detail:

Step i) A common parametrisation (d_{ij}) of the Kramers-Moyal coefficients is a linear function for $D^{(1)}$ and a parabolic function for $D^{(2)}$

$$D^{(1)}(u_r) = d_{11}(r) u_r, \quad (3.15)$$

$$D^{(2)}(u_r) = d_{22}(r) u_r^2 + d_{20}(r). \quad (3.16)$$

As we will see later, these functions conform well with the shape of $D^{(1)}$ and $D^{(2)}$ (also denoted as $D^{(1,2)}$) constructed from the measurement data.

Step ii) A calculation of $p(u_r|u_{r+l_{EM}})$ is done by the use of the short time propagator (Risken 1984; Renner *et al.* 2001)

$$p_{STP}(u_r|u_{r+l_{EM}}) \approx \frac{1}{\sqrt{4\pi D^{(2)}(u_{r+l_{EM}}) l_{EM}}} \times \exp\left(-\frac{[u_r - u_{r+l_{EM}} - D^{(1)}(u_{r+l_{EM}})l_{EM}]^2}{4D^{(2)}(u_{r+l_{EM}})l_{EM}}\right). \quad (3.17)$$

This particular functional form of eq. (3.17) is reached by implementing the scale step in units of the Einstein-Markov coherence length l_{EM} , which has the advantage that the short time propagator only depends on $D^{(1,2)}$.[†]

Since the experimentally found conditional PDFs $p_{exp}(u_r|u_{r+l_{EM}})$ become noisy at large values of u_r and $u_{r+l_{EM}}$, it is better to use the joint PDFs for the optimisation procedure. Therefore, conditional PDFs $p_{STP}(u_r|u_{r+l_{EM}})$ from eq. (3.17) are converted by Bayes' theorem to joint PDFs $p_{STP}(u_r; u_{r+l_{EM}})$.

Step iii) Next we set the numerical calculated joint PDF p_{STP} in comparison with the measured reference p_{exp} by the use of a weighted mean square error function in logarithmic space, cf. Feller (1968), (analogous to Kullback-Leibler entropy),

$$\epsilon(p_{STP}, p_{exp}) = \frac{\int_{-\infty}^{+\infty} \int_{-\infty}^{+\infty} (p_{STP} + p_{exp})(\ln(p_{STP}) - \ln(p_{exp}))^2 du_r^2}{\int_{-\infty}^{+\infty} \int_{-\infty}^{+\infty} (p_{STP} + p_{exp})(\ln^2(p_{STP}) + \ln^2(p_{exp})) du_r^2}, \quad (3.18)$$

with \ln as natural logarithm. ϵ is taken as a logarithmic measure for the distance between the distributions.

Step iv) The logarithmic distance ϵ is taken as a cost function for an optimisation procedure. The optimisation procedure systematically changes $D^{(1,2)}$ until ϵ is minimised. The optimisation procedure is a 2nd order method based on a Hessian matrix. We used for this optimisation the function *fmincon* implemented in MATLAB[®] R2012a. The constraints are set in a physically and mathematically meaningful way, $-\infty \leq d_{11} \leq 0$, $0 \leq d_{22} \leq \infty$ and $0 < \delta_d \leq d_{20} \leq \infty$, here $\delta_d = 10^{-3}$.

3.4. Integral fluctuation theorem

Next we present the IFT and its thermodynamic origin as a new physical law for the turbulent cascade, and furthermore, as an independent measure to show the validity of the Markov description of the cascade. In addition, the functional form of the estimated functions $D^{(1,2)}$ is disclosed and assessed by the IFT.

[†] The proper size of a scale step in eq. (3.17) is investigated by the use of the Chapman-Kolmogorov equation, cf. Risken (1984). The specified step size l_{EM} leads to consistent results, smaller steps than l_{EM} do not significantly improve the results

The Kramers-Moyal coefficients describe the turbulent system and its increment trajectories from an initial state given by $p(u_L, L)$ to a *final* state $p(u_\lambda, \lambda)$. The corresponding stochastic process that defines the evolution in scale of an initial increment u_L drawn from $p(u_L, L)$ down to the final increment u_λ can be interpreted as an analogue of a non-equilibrium thermodynamic process. Most importantly, drawing the analogy to non-equilibrium thermodynamics entails the notion of irreversible entropy production for a turbulent cascade, with useful implications. Now, we make a short digression into non-equilibrium thermodynamics to explain the background in more detail.

In non-equilibrium thermodynamics, external forces generate a deterministic drift $D^{(1)}$ and the thermal energy $k_B T$ defines the diffusion function $D^{(2)}$. The drift and the diffusion function are the two ingredients to set up the Fokker-Planck or, equivalently, the Langevin equation of non-equilibrium thermodynamic processes, cf. Lemons (1997), Sekimoto (1998). For a turbulent cascade, the linear drift $D^{(1)}(u_r)$ in eq. (3.15) accounts for the tendency of turbulent structures to split into smaller structures, invoked by the non-linearity of the Navier-Stokes equation.

Drawing the analogy further, just as the thermal movement of the particles of an embedding medium is a source of fluctuations for a system of interest, we interpret u_r^2 as an energetic term being a source of velocity fluctuations throughout the turbulent cascade u_r itself. The functional form of the fluctuation describing coefficient $D^{(2)}(u_r)$ in eq. (3.16) hence suggests that the r -dependency of the $d_{22}(r)$ term constitutes the influence of turbulent energy on small scale intermittency. This interpretation receives support by the role of the energy transfer rate on the cascade, studied in Gagne *et al.* (1994), Naert *et al.* (1997), Renner *et al.* (2002a): Fixing the transferred energy ε to constant values or, equivalently, looking only at cascade trajectories with constant ε , no intermittency is observed and $p(u_r|\varepsilon)$ becomes Gaussian, i.e. $d_{22}(r)$ vanishes. In addition to turbulent energy as source of fluctuations, the coefficient $d_{20}(r)$ procures background fluctuations independent from u_r . We come back to this picture of the turbulent cascade when we discuss our results in section 4.3 and 4.4. For more details on the Markov picture of the cascade process we refer the reader to Nickelsen (2017).

From the energy balance of the thermodynamic Langevin equation follows an expression for the heat exchange with the medium along a single trajectory of the system, cf. Sekimoto (1998). The heat exchange is associated with an entropy production in the medium, S_m , and the change in Gibbs entropy, Δs , which is associated with the change of system entropy. Thus the total entropy production can be defined as $\Delta S = S_m + \Delta s$, cf. Seifert (2005).

As being the entropy production of an isolated system, ΔS must satisfy the second law of thermodynamics, $\Delta S \geq 0$. However, single fluctuations with a tendency against the average behaviour give rise to entropy consumption, $\Delta S < 0$. Therefore, it is important to remember that the second law addresses the macroscopic entropy production, which means that on average the total entropy production is non-negative, $\langle \Delta S \rangle \geq 0$. Fluctuating entropy productions are central in the arising field of stochastic thermodynamics, of which one result are the so-called *fluctuation theorems*. These theorems express the balance between entropy production and entropy consumption by tightening the second law to an equality, cf. Seifert (2012). Here, we are concerned with the *integral* fluctuation theorem (IFT) for the total entropy production, Seifert (2005),

$$\langle e^{-\Delta S} \rangle = 1. \quad (3.19)$$

In order to amount to the average of 1, it is evident that the IFT assigns an exponential weight to the rare entropy consuming fluctuations that contribute with values much larger than 1 to the average, in opposition to the typical entropy producing fluctuations that

contribute with values between 0 and 1. It is this delicate balance between production and consumption of entropy that makes the IFT so useful for the analysis of non-equilibrium systems. Typically, the IFT finds applications in small systems on nano-scale, whereas its applicability is not evident for classical turbulent flows with scales in the range of mm and velocity fluctuations of order m/s.

At this point, we turn to turbulent cascades again and refer the interested reader to the comprehensive review by Seifert (2012) for more details on stochastic thermodynamics. On the basis of single realisations of the cascade process, or, to be explicit, trajectories $u(\cdot) = \{u_r; r = L \dots \lambda\}$, the formal entropy production S_m is given by, cf. Nickelsen & Engel (2013), †

$$S_m[u(\cdot)] = \int_L^\lambda \partial_r u_r \frac{D^{(1)}(u_r, r) - \partial_u D^{(2)}(u_r, r)}{D^{(2)}(u_r, r)} dr. \quad (3.20)$$

The difference in Shannon entropy reads

$$\Delta s(u_L, u_\lambda) = -\ln \frac{p(u_\lambda, \lambda)}{p(u_L, L)}. \quad (3.21)$$

If the drift and diffusion functions $D^{(1,2)}$ that define the cascade process as well as $p(u_L, L)$ and $p(u_\lambda, \lambda)$ are known, the total entropy production for a single trajectory $u(\cdot)$ can formally be determined as the sum of the two contributions mentioned above,

$$\Delta S[u(\cdot)] = S_m[u(\cdot)] + \Delta s(u_L, u_\lambda). \quad (3.22)$$

Suppose $\{u(\cdot)\}$ are exact realisations of a cascade process defined by $D^{(1,2)}$ and $p(u_L, L)$, then $\langle e^{-\Delta S} \rangle$ should converge to exactly 1 for an unlimited number of $u(\cdot)$ taken into account. In Nickelsen & Engel (2013) it has been demonstrated for a single set of data from a free jet experiment that the exponential average in the IFT is indeed converging very fast to 1. The crucial requirement for the convergence is the occurrence of rare trajectories with $\Delta S < 0$. Nickelsen & Engel (2013) found that the trajectories with $\Delta S < 0$ exhibit an *increase* of fluctuations when evolving from L to λ , against the typical tendency of the cascade. It is, hence, the phenomenon of small scale intermittency that is responsible for the applicability of the IFT to turbulent cascades and its convergence. However, a universal form of $D^{(1,2)}$ and therewith a universal form of the IFT is still missing. So is, e.g., the exponential average of the IFT deriving from the K62 model eq. (3.5) diverging rapidly for the data of the free jet experiment considered in Nickelsen & Engel (2013), confirming the well known fact that the K62 model does not reflect properly small scale intermittency of real turbulent flows. For the discussion of other models of turbulence see Nickelsen (2017).

Here, we extend the investigations done in Nickelsen & Engel (2013) substantially and for the first time employ the utility of the IFT to explore the role large scale structures play for small scale turbulence. In doing so, we address three points. First of all, we show that the IFT holds for all different types of turbulent flows considered here and thus collect strong evidence that the IFT is a universal feature of turbulence. Secondly, the high sensitivity of the IFT regarding realistic modelling of small scale intermittency enables us to verify our estimation of $D^{(1,2)}$ and to quantify the importance and significance of different functional contributions of $D^{(1,2)}$. And finally, the interpretation as a non-equilibrium thermodynamic process illuminates the role of these functional contributions in terms of small scale intermittency and universality.

† Here, we deviate from the previous suppression of the argument r to stress the explicit r -dependency of $D^{(1,2)}(u_r, r)$ and $p(u_r, r)$

To test the quality of the estimated functions $D^{(1,2)}$, we extract n trajectories $\{u(\cdot)\}$ from each of the measured flow fields $v(x)$ by applying the definition eq. (3.2) for different values of x . To ensure the independence of the trajectories, we take equidistant values for x with step size L , owing to the fact that L specifies the size of the largest coherent structures in $v(x)$. For each set of trajectories, $\{u(\cdot)\}$, we calculate a set of total entropy productions $\{\Delta S_j\}$ from eq. (3.22) in order to employ the IFT by

$$1 = \left\langle e^{-\Delta S[u(\cdot)]} \right\rangle \simeq \frac{1}{n} \sum_{j=1}^n e^{-\Delta S_j} =: I(n). \quad (3.23)$$

The overall implementation of the IFT is then as follows. For each of the datasets considered here, $D^{(1,2)}$ are estimated and used to define the form of S_m in eq. (3.20), $p(u_L, L)$ and $p(u_\lambda, \lambda)$ are estimated to define Δs in eq. (3.21), and the very data that was used for this estimation is plugged into the IFT. If the IFT is confirmed, the Markov process defined by $D^{(1,2)}$ and the initial condition $p(u_L, L)$ correctly captures the cascade process and in particular the small scale features of the turbulent flow. In addition to this quality check, the IFT serves as a clear cut criterion to pin down and discuss the minimal functional form of $D^{(1,2)}$ that still captures the cascade process.

4. Results

In this section, we show the results obtained from all 61 datasets. The analysis of structure functions sets our data into the common picture of turbulence and checks if the data obeys a scaling law. Subsequently, we demonstrate and discuss the validity of the IFT and our parametrisation of the Kramers-Moyal coefficients, followed by a discussion of their functional form. Thereafter, results of multi-scale statistics are presented and discussed in the context of universal and non-universal flow dependencies of turbulence.

4.1. 2-point scaling features

We begin with the standard analysis of our data. Figure 1 presents second ($\kappa = 2$) and fourth order ($\kappa = 4$) structure functions according to eq. (3.3) obtained from all datasets. The lower band corresponds to second and the upper band corresponds to fourth order structure functions. The greyscale of the curves indicates the Taylor Reynolds numbers. It is clearly seen how the *scaling range* increases with Re_λ . Structure functions are normalised in their scale and in their values by Θ and σ_Θ , defined in section 3.1. The band of the fourth order structure functions is shifted by a factor of 10 along the ordinate axis for reasons of presentation. The norms Θ and σ_Θ are shown in appendix A3 as functions of Re_λ . These norms are dimensional and show features which depend also on the flow type.

For a more precise analysis of the scaling behaviour of the structure functions, we present in Figure 2 a) the local scaling exponent $\xi_2(r)$ according to eq. (3.6). Due to our normalisation, all datasets pass through $\xi_2 = 0.696$ at $\frac{r}{\Theta} = 1$. Three curves are marked by symbols to indicate that $\xi_2(r)$ changes from a linear behaviour for low Re_λ to a power 5 behaviour for high Re_λ (with respect to the log-log presentation). This shows that the local scaling exponent flattens with increasing Re_λ around $\xi_2 = 0.696$. Thus, instead of a stretched constant scaling range, only a tendency to usual scaling † behaviour is seen, even for the highest Re_λ datasets.

For the third and fourth order structure function, similar results are shown in Sinhuber

† With usual scaling we refer to the case that no functional deviation from a scaling law is present, i.e. $\xi_\kappa(r)$ is rigorously constant in r , e.g. eq. (3.5)

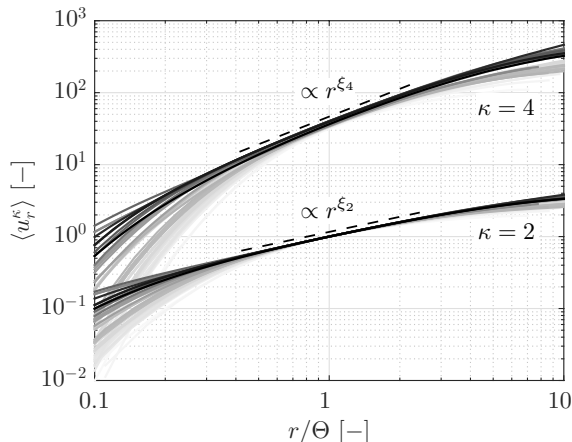


FIGURE 1. Second ($\kappa = 2$, lower band) and fourth ($\kappa = 4$, higher band) order structure functions versus normalised scale. The whole band of the fourth order structure functions is shifted by a factor of 10 for reasons of presentation. The greyscale used for the curves indicates corresponding Taylor Reynolds numbers, bright grey to black corresponds to increase of Re_λ .

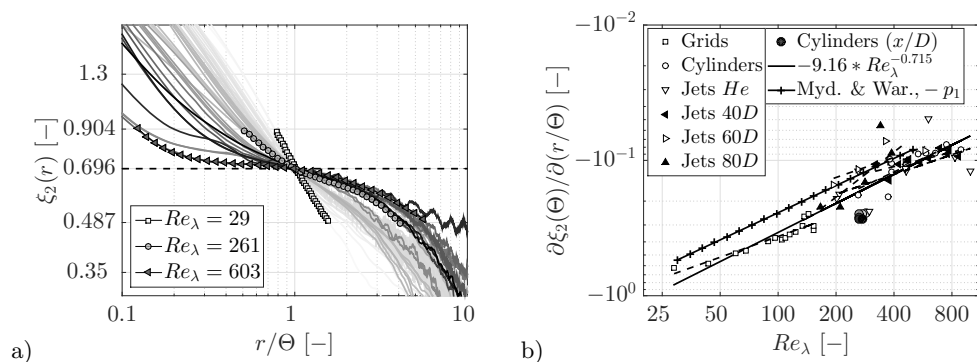


FIGURE 2. a) Local second order scaling exponent $\xi_2(r)$ according to eq. (3.6) in a double-logarithmic plot. Presentation alike figure 1. b) Slope of local second order scaling exponent $\xi_2(r)$ at $r = \Theta$ in a double-logarithmic presentation together with data from Mydlarski & Warhaft (1996)

(2015, pp. 121-122, fig. 4.3 and 4.4) and Sinhuber *et al.* (2017) and confirm the flattening of structure functions for even higher Re_λ for grid generated turbulence, also Grauer *et al.* (2012) used a similar approach. An explanation of this non perfect scaling behaviour of structure functions is that finite size effects play a role, Dubrulle (2000), which also supports the idea of introducing the specific scale Θ defined in section 3.1.

Figure 2 b) shows the slope of the local second order scaling exponent $\xi_2(r)$ at $r = \Theta$ as function of Re_λ . This slope is obtained by fitting a polynomial of 5th order as shown in figure 2 a). The solid line shows the trend of all datasets with the functional form of

$$\frac{\partial \xi_2(\Theta)}{\partial (r/\Theta)} \approx -9.16 Re_\lambda^{-0.715}. \quad (4.1)$$

Based on this result, $\partial_{(r/\Theta)} \xi_2(\Theta)$ can be proposed as an alternative to Re_λ .

Additional data from a similar study done by Mydlarski & Warhaft (1996) is added to figure 2 b). This data represents a deviation from the common energy density spectra

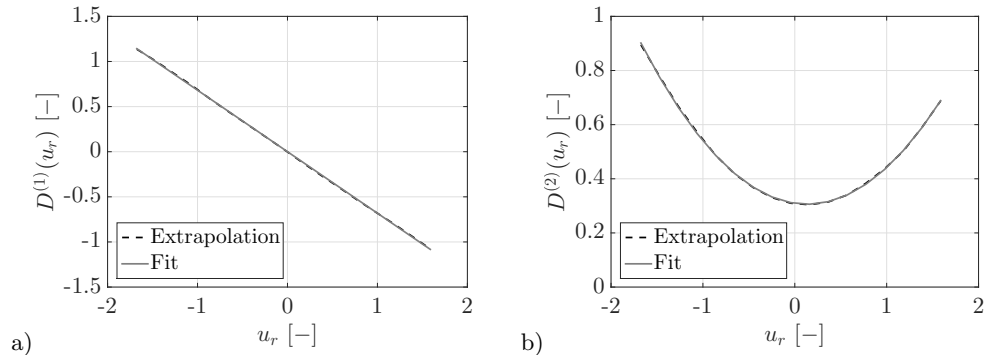


FIGURE 3. $D^{(1,2)}$ versus u_r , according to eq. (3.14) and higher order corrections, cf. Gottschall & Peinke (2008). Linear and parabolic fitting functions illustrate their functional forms. The dataset *jet 1* (table 1) is used at $r = 1l_{EM}$.

scaling $E(k) \propto k^{-5/3}$ †. The deviation is expressed by p_1 in the form of $E(k) \propto k^{-(5/3-p_1)}$. Turbulent flows and their $E(k)$ are investigated up to $Re_\lambda \leq 500$. They found that p_1 has the form $p_1 = 5.25Re_\lambda^{-2/3}$, which is very similar to the Re_λ -dependence we found in eq. (4.1). The pre-factor differs due to the different approaches.

4.2. Estimation procedure of Kramers-Moyal coefficients

We now extend our analysis to joint multi-scale statistics. The first estimation of Kramers-Moyal coefficients is based on conditional moments and their extrapolation. Figure 3 a) and b) exemplarily show $D^{(1)}$ and $D^{(2)}$ as functions of u_r according to eq. (3.14) and higher order corrections, cf. Gottschall & Peinke (2008). A linear and a parabolic fitting function reflect the common functional forms of $D^{(1,2)}$, which are used for the subsequent optimisation. The used fit range is indicated, $-1.5 \leq u_r \leq 1.5$. Here one might argue that higher order contributions can be seen in $D^{(1,2)}$ (compared to the approach in eq. (3.15) and (3.16)). We come back to this point when we discuss the results regarding the IFT.

As a second step for the estimation of Kramers-Moyal coefficients, the optimisation procedure of Chapter 3.3 is applied. This procedure is based on the reconstruction of PDFs according to eq. (3.17). Figure 4 shows the quality of reconstructed conditional PDFs by the optimised Kramers-Moyal coefficients at two different scales, $r = l_{EM}$ and $r = 60l_{EM}$. To pronounce the differences, we have chosen $r = 60l_{EM}$ which corresponds to a scale larger than L . The agreement of experimental and reconstructed conditional PDFs is good.

In order to further show the quality of the reconstructed conditional PDF, we analyse the change of conditional PDFs along the scale, cf. eq. (3.9) and (3.10). Figure 5 shows the cumulative change of conditional PDF, expressed as

$$\begin{aligned} \delta p &= [p(u_{l_{EM}}|u_{2l_{EM}}) - p(u_{2l_{EM}}|u_{3l_{EM}})] \\ &+ [p(u_{2l_{EM}}|u_{3l_{EM}}) - p(u_{3l_{EM}}|u_{4l_{EM}})] \\ &+ \dots \\ &+ [p(u_{(N-1)l_{EM}}|u_{Nl_{EM}}) - p(u_{Nl_{EM}}|u_{(N+1)l_{EM}})] \end{aligned} \quad (4.2)$$

$$= p(u_{l_{EM}}|u_{2l_{EM}}) - p(u_{Nl_{EM}}|u_{(N+1)l_{EM}}). \quad (4.3)$$

† Note that second order structure functions and energy density spectra contain the same information and can be converted into each other by Fourier transformation

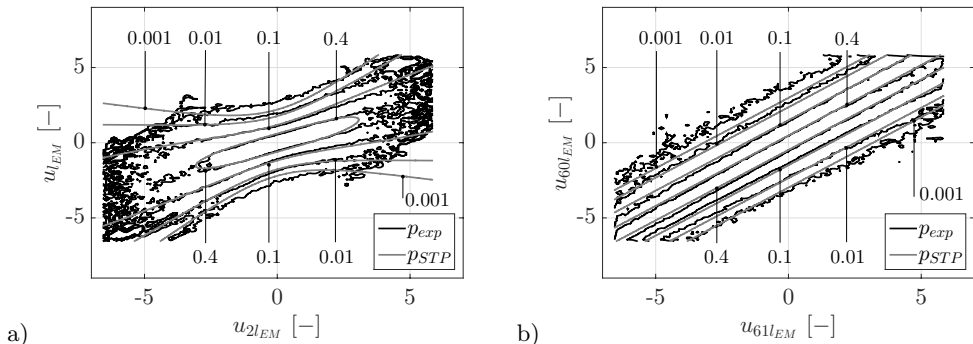


FIGURE 4. Contour plots show experimental and reconstructed conditional PDFs at two different scales, a) $r = l_{EM}$ and b) $r = 60l_{EM}$. A dataset of subgroup (v) is used with $Re_\lambda = 475$.

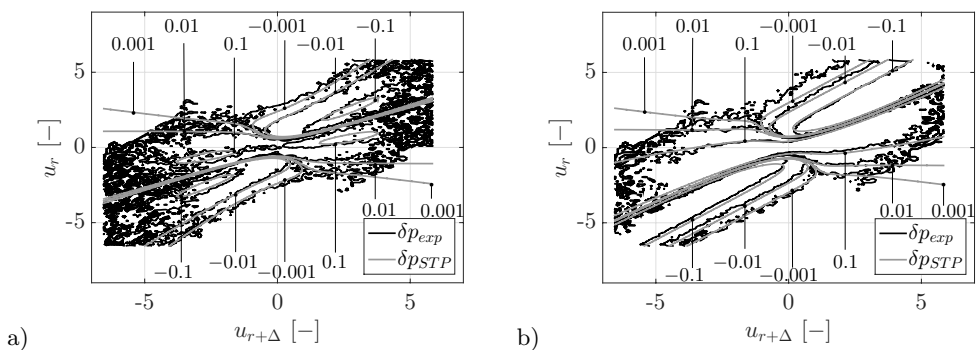


FIGURE 5. Change of conditional PDF δp along the scale. a) δp for $N = 2$, which corresponds to small scale change and b) for $N = 60$, which corresponds to the entire change within inertial range. A dataset of subgroup (v) is used with $Re_\lambda = 475$.

In figure 5, δp_{exp} corresponds to the cumulative change of experimental data and δp_{STP} is deduced by means of the short time propagator, eq. (3.17), and the optimised Kramers-Moyal coefficients. Due to the scale-wise optimisation procedure, eqs. (4.2) and (4.3) are not necessarily equal for the reconstructed PDFs, thus we use eq. (4.2). Figure 5 a) shows δp for $N = 2$ (the change of the cPDFs at small scales) and figure 5 b) presents δp for $N = 60$ (the change of the cPDFs over a broad range of scales). We see in both figures that the distributions of δp_{exp} and δp_{STP} are in good agreement. Thus, the optimisation procedure works well from the smallest scale changes $\delta r = l_{EM}$ up to the cumulative change of the entire inertial range. Consequently, we assume that the description of the turbulent cascade process is properly characterised by optimised Kramers-Moyal coefficients.

It is a very strong demand on the quality of the reconstructed Kramers-Moyal coefficients to show that the cPDFs are well reproduced. Naturally, also the commonly investigated increment PDFs $p(u_r)$ and the structure functions are reproduced well by these optimised stochastic equations. As the third order structure function S^3 with its four-fifth law plays a key role for turbulence, we show exemplarily for one dataset in figure 6 the comparison of S^3 between the result of the Fokker-Planck equation and the measured one. For further discussion see later on.

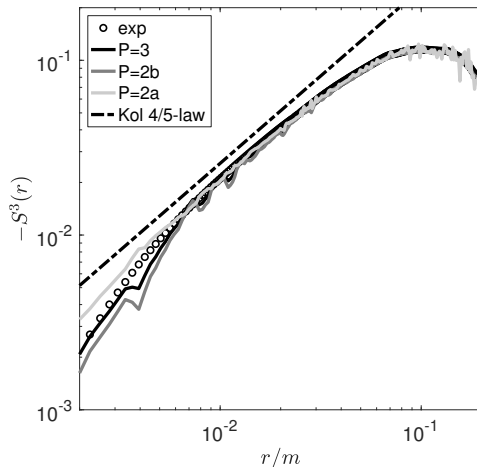


FIGURE 6. Third order structure function $-S^3$ as a function of scale r/θ . Shown are the results obtained from the experimental data (exp) and for different functional forms of the Kramers-Moyal coefficients corresponding to the cases of table 2. In addition the four-fifth law is shown. The dataset of subgroup vii is used with $Re_\lambda = 166$.

4.3. General validity of the integral fluctuation theorem and parametrisation of $D^{(1,2)}$

As a next step, we first demonstrate the validity of the IFT for our datasets and then employ the IFT to assess the quality of the optimised Kramers-Moyal coefficients and discuss their functional contributions.

Figure 7 presents the IFT for all datasets as a function of the number n of considered velocity increment trajectories $u(\cdot)$ as stated in eq. (3.23). Here we used again the optimised functions $D^{(1,2)}$. Due to different numbers of samples in the datasets and varying Taylor micro-scale as well as integral length scales, the maximal number of independent trajectories differ from dataset to dataset. The four selected datasets from table 1 are highlighted by symbols, other datasets are shown in grey. At $n \approx 1000$, $I(n)$ has already largely converged to 1, eq. (3.23), and only slight improvements of convergence are present at larger number of trajectories, $n > 1000$. The average of the 61 IFT values taken at $n = \text{maximal}$ is $\langle I_{\text{max}} \rangle_{\text{datasets}} \approx 1.01$ and the standard deviation of the 61 I_{max} is $\sigma(I_{\text{max}}) \approx 0.01$, which we take as strong evidence that the IFT is a universal feature of turbulent cascades.

Next we reverse the argumentation and take the IFT as a given fundamental law for the turbulent cascade. Thus we can verify our parametrisation and the significance of functional contributions of $D^{(1,2)}$ can be worked out. To test these aspects we parametrise $D^{(1,2)}$ up to third order in u_r †, i.e. with 8 parameters,

$$D^{(1)}(u_r) = d_{13}(r)u_r^3 + d_{12}(r)u_r^2 + d_{11}(r)u_r + d_{10}(r), \quad (4.4)$$

$$D^{(2)}(u_r) = d_{23}(r)u_r^3 + d_{22}(r)u_r^2 + d_{21}(r)u_r + d_{20}(r). \quad (4.5)$$

The parameters d_{ij} are continuous functions of r which is advantageous for the determination of $I(n)$. To single out the important parameters among the d_{ij} above, the number of parameters has successively been reduced from 8 to 2 as shown in table 2. Figure 8 presents this investigation for one exemplary dataset (subgroup (v), $Re_\lambda = 475$). For each selection of parameters the above mentioned optimisation procedure to determine

† Preliminary investigations with even higher order parametrisations do not show any improvements or other features to this third order approach

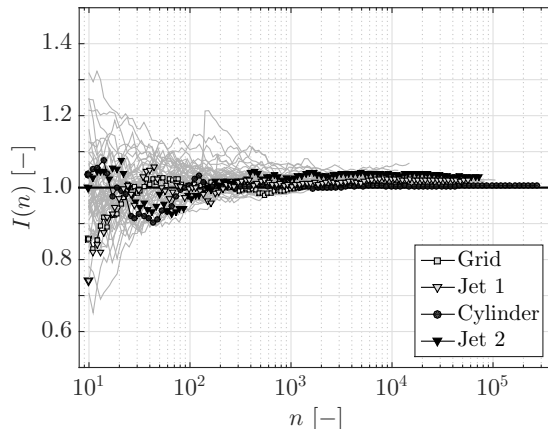


FIGURE 7. IFT according to eq. (3.23) as a function of the number of trajectories n . Results from all data; the selected datasets from table 1 are highlighted by symbols, all other datasets are shown as grey lines.

P	d_{13}	d_{12}	d_{11}	d_{10}	d_{23}	d_{22}	d_{21}	d_{20}	I_{\max}
2a	-	-	X	-	-	-	-	X	$1.3(46) \pm 0.016$
2b	-	-	X	-	-	X	-	-	∞
3	-	-	X	-	-	X	-	X	$1.0(17) \pm 0.016$
4	-	-	X	X	-	X	-	X	$1.0(17) \pm 0.016$
5	-	-	X	X	-	X	X	X	$1.0(18) \pm 0.016$
6	-	X	X	X	-	X	X	X	$1.0(21) \pm 0.016$
7	X	X	X	X	-	X	X	X	$1.0(21) \pm 0.016$
8	X	X	X	X	X	X	X	X	$1.0(24) \pm 0.016$

TABLE 2. Scheme of the chosen parameters d_{ij} for $D^{(1,2)}$ according to eqs. (4.4) and (4.5). On the left row the number of used parameters are given. Crosses indicate non-zero parameters. The corresponding I_{\max} values are given with their uncertainties.

$D^{(1,2)}$ was repeated and the IFT was tested. The resulting values I_{\max} are shown in table 2. We estimate an error of the I_{\max} by considering the convergence of the IFT ($1000 \leq n \leq \text{maximal}$) and its fluctuations around the saturation value I_{\max} , figure 8. In accordance with the mentioned standard deviation ($\sigma(I_{\max}) \approx 0.01$), the estimated error is 0.016. From the results presented in table 2 and in figure 8 we conclude that different functional representations of $D^{(1,2)}$ are possible to fulfil the IFT in good quality.

Next we discuss the meaning of the single cases. The case $P = 2a$ in table 2 corresponds to pure additive noise in the cascade process. This implies only Gaussian increment PDFs, i.e. no intermittency is taken into account. The value of $I_{\max} = 1,3(46)$ and the large jumps with n evidently suggest that the IFT cannot be fulfilled with this functional ansatz, see figure 8. The jumps in the convergence are a consequence of an unbalanced weight on entropy consuming trajectories in the exponential average of the IFT. We consequently reject the case $P = 2a$ as a functional form of $D^{(1,2)}$.

The case $P = 2b$ corresponds to pure multiplicative noise in the cascade process which includes a quadratic term in the diffusion function $D^{(2)}$. Note that this parametrisation corresponds to a generalisation of the scaling proposed by Kolmogorov (1962),

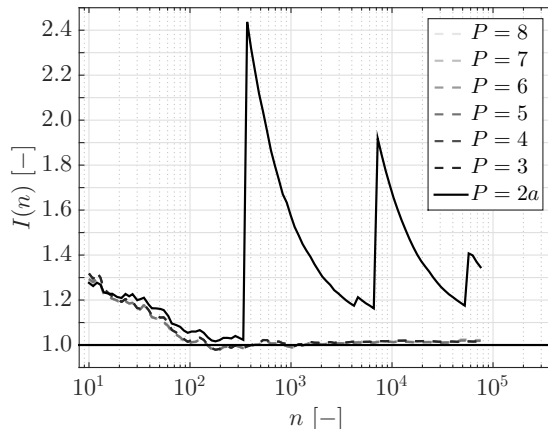


FIGURE 8. IFT, according to eq. (3.23), as function of the number of trajectories n for different parametrisation of $D^{(1,2)}$ according to table 2. Note that $P = 2b$ is not shown in figure 8, since the IFT diverges for this case.

see eq. (3.5) and Friedrich & Peinke (1997a), Nickelsen & Engel (2013). As the IFT diverges, this functional form is rejected as well.

For all the other choices with three and more parameters ($P \geq 3$), we see good fulfilment of the IFT. More coefficients do not lead to a significantly better fulfilment of the IFT and its convergence. We hence conclude that the case $P = 3$ is sufficient for a good stochastic model of the turbulent cascade that captures the features of small scale intermittency. Higher order terms as used in Renner *et al.* (2001) and Nickelsen & Engel (2013) seem not to be necessary. Similar stochastic models have been discussed before, see e.g. Dubrulle (2000) and Laval *et al.* (2001). Starting with the Navier-Stokes equation, Laval *et al.* derive after certain simplifications and approximations a Langevin equation with correlated additive and multiplicative noise, which is of similar but more involved form as our case $P = 3$. The amplitude of the additive noise is related to our d_{20} term, and the amplitude of the multiplicative noise to the d_{22} term. The conceptual difference, however, is that in Laval *et al.* (2001) the skewness is generated by the correlation between the two noise sources, which would imply a linear term d_{21} (case $P = 5$), whereas in our model the skewness already present at integral length scales is taken and transported down the cascade by the deterministic $d_{11}(r)$ term. This can also be seen in figure 6 where already the additive or the multiplicative noise alone are enough to reproduce the measured skewness (cases $P = 2a$ and $P = 2b$), as long as the linear drift term d_{11} is part of the model.

To conclude, we see that the minimal functional form to fulfil the IFT is for $D^{(1)}$ a linear term, $d_{10}(r)u_r$, and for $D^{(2)}$ an additive term $d_{20}(r)$ as well as a quadratic term $d_{22}(r)u_r^2$, which is in accordance with eq. (3.15) and (3.16) †. We also recognised that d_{22} becomes increasingly important for the fulfilment of the IFT with increasing Re_λ , indicating that small scale intermittency becomes more dominant at higher Re_λ .

The need of the three parameters can also be discussed in the context of structure functions, see Section 3.2 and eq. (3.11). Inserting the three parameters and a multiplication

† Renner *et al.* (2002a) interpreted $d_{20} \neq 0$ and $d_{22} \neq 0$ as a necessary combination for turbulence and its energy cascade

by $-\frac{1}{S^\kappa}$ (from the left) lead to

$$\xi_\kappa = \frac{r}{S^\kappa} \frac{\partial S^\kappa}{\partial r} = -r\kappa \left(d_{11}(r) + (\kappa - 1) \left(d_{22}(r) + \frac{S^{\kappa-2}(r)}{S^\kappa(r)} d_{20}(r) \right) \right). \quad (4.6)$$

Here, we used the substitution $\frac{r}{S} \frac{\partial S}{\partial r} = \frac{\partial \ln(S)}{\partial \ln(r)} = \xi_\kappa(r)$.

Note that the coupled set of differential equations (4.6) is closed: All structure functions can be determined successively from $S^0 = 1$ and $S^1 = 0$. It is obvious that if more parameters were needed, eq. (4.6) becomes more complicated. In the case of negligible d_{20} , eq. (4.6) is an analytic expression for $\xi_\kappa(r)$ and can be transformed to a form comparable to Kolmogorov's expression of the scaling exponent, eq. (3.5), if $d_{11}(r)$ and $d_{22}(r)$ depend reciprocally on r , cf. Renner *et al.* (2001), Nickelsen (2017). This special case also recovers the four-fifth law $\xi_3 = 1$, cf. Kolmogorov (1941). Since the four-fifth law is only exact for the *ideal* case of homogeneous and isotropic turbulence at infinite Reynolds numbers, we do not expect that the four-fifth law is identically reproduced by our analysis of *real* experimental data. The deviation from the four-fifth law rather accounts for corrections that are mandatory for realistic turbulent flows, similar to the widely accepted approach of extended self-similarity introduced by Benzi *et al.* (1993, 1996). For one exemplarily chosen dataset we have shown in figure 6 the resulting third order structure functions. Even for the cases $P = 2a$ and $P = 2b$ the third order structure function is well reproduced. This result does not put the importance of the negative skewed statistics of the velocity increment expressed by S^3 into question, but we see quite different Kramers-Moyal coefficients can be used to reproduce S^3 . This is easily understood as structure functions (as well as the PDFs $p(u_r)$) are only two point or one scale quantities and result from a projection of the multi-scale statistics. Thus there are whole families of Fokker-Planck equations that can reproduce these structure functions. Note that depending on the d_{ij} terms, other structure functions, like S^2 via d_{21} , may contribute to the r -dependence of S^3 , otherwise $S^3(r)$ is a relaxation process of the initial large scale skewness $S^3(L)$. This is easily derived from eq. (3.11) and 4.6).

The consistency of the determined coefficients with the measured structure functions is shown in appendix A4.

4.4. The turbulent cascade in terms of Kramers-Moyal coefficients

Based on the results in section 4.3, we take the *simplest* functional form of the Kramers-Moyal coefficients, eq. (3.15) and (3.16), and discuss to what extent the parameters $d_{11}(r)$, $d_{20}(r)$ and $d_{22}(r)$ behave in a universal way with respect to Taylor-Reynolds number and flow type.

Before we discuss the results in detail, we analyse in figure 9 the topological changes of the conditional PDFs with varying scale, which will serve us as a basis for the interpretation of the parameters $d_{11}(r)$, $d_{20}(r)$ and $d_{22}(r)$. Figure 9 a) shows an exemplary conditional PDF at a small scale, $r = l_{EM}$. The maximum of the distribution is located at a diagonal of the form $d : u_r = cu_{r'}$, which is referred to as *distribution diagonal* or simply *diagonal*. Figure 9 a) shows that at scale $r = l_{EM}$ the distribution diagonal is $d : u_{l_{EM}} = 0.5u_{2l_{EM}}$. The contour isolines are curved beneath and above this diagonal.

Figure 9 b) shows for the same dataset the conditional PDF at larger scale, $r = 60l_{EM}$.[†] The distribution diagonal is now roughly at $d : u_{60l_{EM}} = u_{61l_{EM}}$. The contour isolines are not curved but almost parallel to the diagonal.

[†] To pronounce the differences between small and large scale, $r = 60l_{EM}$ is chosen larger than L

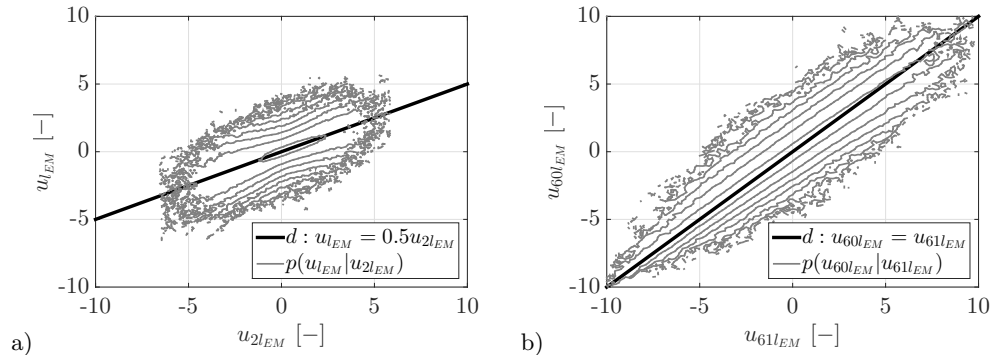


FIGURE 9. a) Conditional PDF at $r = l_{EM}$. The location of the diagonal of the cPDF is indicated by the function $d : u_{l_{EM}} = 0.5u_{2l_{EM}}$. b) Conditional PDF at $r = 60l_{EM}$, the diagonal function is $d : u_{60l_{EM}} = u_{61l_{EM}}$. For a) and b) a dataset of subgroup (v) is used with $Re_\lambda = 475$.

These changes in conditional PDF shape can be related to the parameters by considering the short time propagator, eq. (3.17). The leading term for the maximum is given by $D^{(1)}$ and d_{11} . The smaller the magnitude of d_{11} , the more the diagonal approaches $d : u_r = u_{r+l_{EM}}$. The width w of the distribution around the diagonal is proportional to the denominator in the exponential term of eq. (3.17), $w \propto d_{20} + d_{22} u_{r+l_{EM}}^2$. Thus, the coefficient d_{22} expresses the non-linearity in the standard deviation and gives rise to the curvature of the contour isolines: The lower d_{22} , the smaller the curvature will be. In terms of unconditional PDF, a large d_{22} is equivalent to fat-tailed increment distributions, confirming the previous interpretation that intermittent fluctuations are caused by d_{22} . At $u_{r+l_{EM}} = 0$, only d_{20} characterises the width of the distribution. Further details are discussed in appendix A5.

Now, we return to the results of the three parameters d_{11} , d_{22} and d_{20} and their scale dependence. In figure 10, these parameters are shown as a function of the scale r and the Taylor-Reynolds number Re_λ for grid generated turbulence. Grid data was selected, because for this data the smallest scattering was observed. The same presentation of the parameters for cylinder and free jet flows are shown in appendix A6.

Figure 10 a) shows the convergence of all d_{11} to the fixed value $d_{11} = -0.5$ at $r = l_{EM}$, which corresponds to a distribution diagonal $d : u_r = 0.5u_{r+l_{EM}}$, like figure 9 a). Furthermore, all d_{11} are approximately linear at small scales in the log-log presentation. Thus, d_{11} can be expressed according to

$$d_{11} \approx -0.5 \left(\frac{r}{l_{EM}} \right)^{-\frac{1}{2}}. \quad (4.7)$$

Eq. (4.7) is found to hold universally for all types of flows, as shown in appendix A6. The exponent $-\frac{1}{2}$ is in accordance with an earlier indication of Renner *et al.* (2002b) for free jet flows. At larger scales, $r \geq 4l_{EM}$, the slope of d_{11} decreases slightly and deviations from the power law become visible. The higher Re_λ , the larger the scale where the deviation from the power law sets in. Thus, eq. (4.7) indicates that the case $d : u_r = u_{r+l_{EM}}$ is reached only at very large scales and in the limit of very large Re_λ .

Furthermore, the power law with negative exponent eq. (4.7) implies an accelerating decay of turbulent structures along the cascade. From a uniform cascade process, as in the K62 model eq. (3.5), one would expect the power law exponent for d_{11} to be -1 with a prefactor ≈ -0.36 , cf. Friedrich & Peinke (1997a), Nickelsen (2017). Compared to the K62 process, the smaller exponent $-1/2$ found in our analysis together with the

prefactor -0.5 constitutes a decelerated decay of turbulent structures towards smaller scales.

Figure 10 b) presents d_{20} in a semi-logarithmic plot. All d_{20} show a similar functional form with an increase in scale and with a small monotone curvature. The Re_λ -dependency is rather weak. The functional form can be approximated by

$$d_{20} \approx (\alpha_{20} \ln(\frac{r}{l_{EM}}) + \beta_{20})^{\frac{1}{3}}, \quad (4.8)$$

where α_{20} and β_{20} are fit parameters, see also appendix A4 and figure 16 c). Accordingly, background fluctuations decrease moderately to smaller scales.

Figure 10 c) presents d_{22} in a semi-logarithmic plot. All d_{22} decrease strongly with increasing scale, with a slower decrease for increasing Re_λ . This functional behaviour can be approximated by

$$d_{22} \approx \alpha_{22} \ln(\frac{r}{l_{EM}}) + \beta_{22}, \quad (4.9)$$

where α_{22} and β_{22} are fit parameters, see also appendix A4 and figure 16 b). In contrast to d_{20} , d_{22} increases strongly to smaller scales. Since d_{22} is the magnitude of the u^2 term in $D^{(2)}$, intermittent features also increase towards smaller scales, establishing the link to small scale intermittency.

The above parametrisation also allows a qualitative discussion of the infinite Reynolds number limit. From figures 10, 12 and 19 - 21 it can be concluded that d_{11} and d_{20} appear to be rather independent from Re_λ . For d_{11} , this independence is apparent, for d_{20} one may also see a decreasing tendency with Re_λ which was also found in Renner *et al.* (2002a). In contrast, d_{22} clearly increases with Re_λ , confirming that small scale intermittency intensifies with Re_λ . A direct quantitative analysis in terms of the intermittency factor μ is questionable due to non-scaling behaviour, Renner *et al.* (2002a, figure 4b), but qualitatively it follows from (3.11) that $\mu(r) = 18d_{22}(r)$, neglecting d_{20} and taking d_{11} and d_{22} as K62 contribution. The resulting local intermittency factor, $\mu(r)$, indeed increases with Re_λ from $\mu = 0.2$ to $\mu = 0.4$ at $r = l_{EM}$, and from $\mu = 0.1$ to $\mu = 0.3$ at $r = 3l_{EM}$, in qualitative agreement with the universal value of $\mu \approx 0.26$.

We continue with an analysis regarding the universality of the functional forms of d_{11} , d_{20} and d_{22} . Figure 11 shows the three parameters for all datasets in logarithmic plots. The parameters are sorted in three groups which reflect the different turbulent flow types. All parameters which belong to grid flows, to cylinder flows or to free jet flows are covered by a surface with different greyscale and are enclosed by different symbols. Dashed lines indicate where edges are overlaid. In addition, figure 12 shows the parameters as function of the Taylor-Reynolds number at the fixed scales $r = l_{EM}$ and $r = 4l_{EM}$.

At small scales, all d_{11} converge to an approximate power law with the exponent -0.5 at $r \gtrsim l_{EM}$, as shown in figure 11 a). Therefore, universal scaling features of d_{11} are found for our datasets at small scales, which is confirmed by plotting the Re_λ -dependence of $d_{11}(r = l_{EM})$, see figure 12 a). At larger scales, the three groups broaden differently and start to deviate from the power law behaviour. Figure 12 b) indicates that the different behaviour in d_{11} is mainly a Re_λ effect and does not show significant differences for the different flows. More specifically, at small scales d_{11} acquires a universal form, which shows neither a dependence on the kind of turbulent flow nor on Re_λ , and at larger scales, Re_λ becomes important, but the kind of flow does not have a strong effect on d_{11} features.

Figure 11 b) shows d_{20} . The three groups of flows increase with scale in a similar manner as for d_{11} . As a further characterisation, we show the Re_λ -dependence of d_{20} again for the same two scales in figures 12 c) and d). The overall trend of the entire

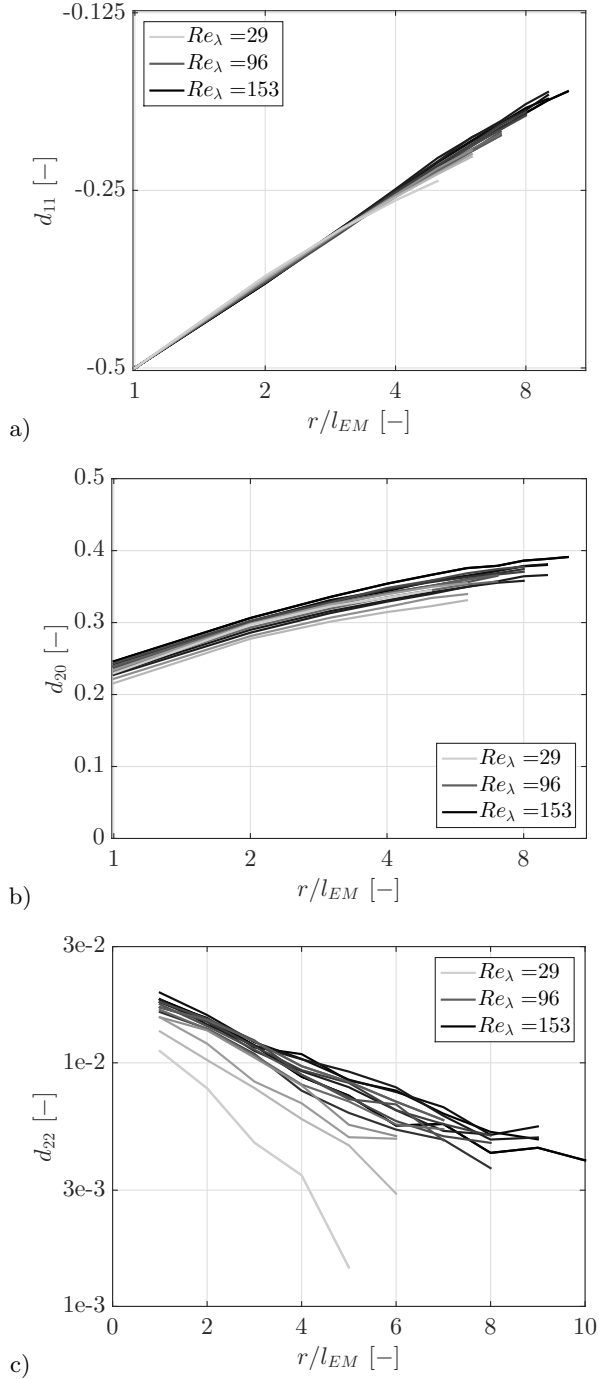


FIGURE 10. Parameters of grid generated turbulence as function of scale. The greyscale indicates Re_λ . a) shows d_{11} in a double-logarithmic plot. b) shows d_{20} in a semi-logarithmic plot. c) shows d_{22} in a semi-logarithmic plot.

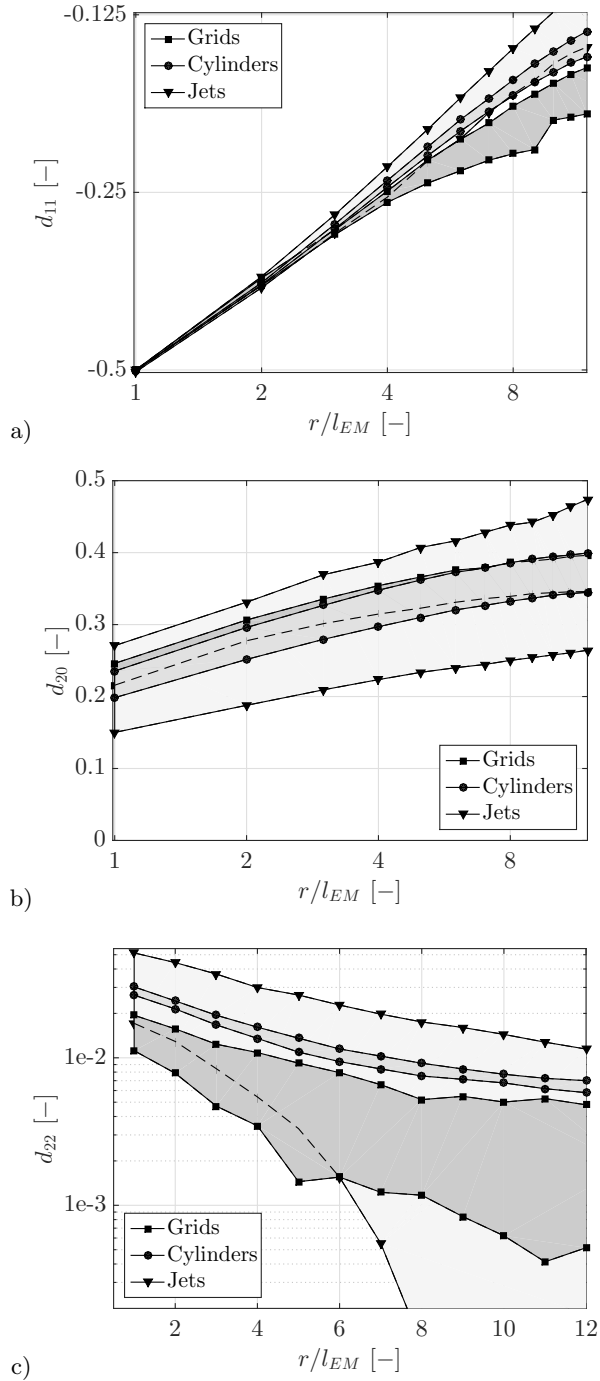


FIGURE 11. Parameters (d_{11} , d_{20} and d_{22}) as function of scale. Surfaces indicate areas where the parameters of specific turbulent flow are located. a) shows d_{11} in a double-logarithmic plot. b) shows d_{20} in a semi-logarithmic plot. c) shows d_{22} in a semi-logarithmic plot.

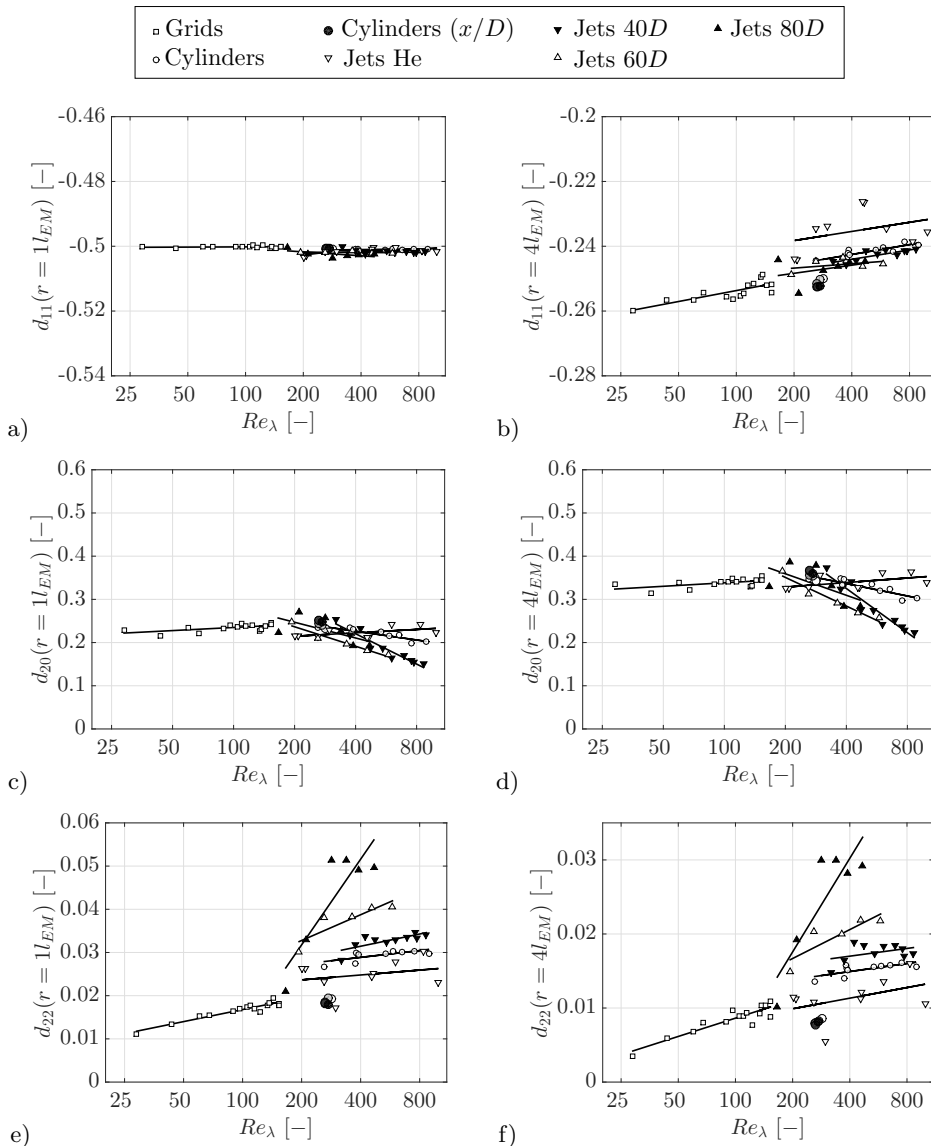


FIGURE 12. Parameters as function of Re_λ at two fixed scales ($r = l_{EM}$ and $4l_{EM}$). Additionally, *linear* fit functions indicate trends. All plots are semi-logarithmically plotted.

datasets is rather constant and subgroups overlap. Thus, a quite uniform band of data is found. Note that d_{20} is sensitive to the normalisation of the velocity increment series, eq. (3.7). On the one hand, a more sophisticated norm based on d_{20} might result in a perfect collapse of the $d_{20}(r)$, at least at one scale. On the other hand, a norm $\sigma_\infty = \sqrt{2}\sigma(v)$ would lead to a distinct dependence of d_{20} on Re_λ . We hence stick to the normalisation using Θ and σ_Θ to deliver a uniform picture in the 2-point and multi-point analysis, which entails the displayed weak dependence of d_{20} on Re_λ , and which therefore supports our choice to use the new quantities Θ and σ_Θ for normalisation.

Regarding d_{22} , the turbulent flows divide into distinct groups, as shown in figure 11 c). These groups are different in shape and broadness, where, from bottom to top, the

functional form of the group's borders changes in a quite systematic way. To investigate whether this behaviour can be explained by a Re_λ -dependence or not, we proceed as above by plotting $d_{22}(r = l_{EM})$ and $d_{22}(r = 4l_{EM})$ as a function of Re_λ , see figures 12 e) and f). In contrast to the findings of d_{11} and d_{20} , the data does not collapse on a uniform Re_λ behaviour, but clearly distinct dependencies can be seen. Each dataset seems to follow a different evolution with Re_λ . Most interestingly, this also holds for the case of small scales $r = l_{EM}$, for which a convergence to a flow type independent behaviour should be expected in the common understanding of universal turbulence.

We further extend our research and try to combine the various subgroups of d_{22} . Plotting the parameter d_{22} as a function of the dimensionless length $\frac{L}{\lambda}$ instead of Re_λ may allow to combine the subgroups within the flow types, i.e. free jet data becomes more aligned, see figure 22 in appendix A7. However, the different flow types itself cannot be combined to one universal functional form.

5. Conclusion

In the common understanding of turbulence, large scale structures, where energy is fed into a cascade process, are known to be dependent on the generating process. For small structures, it is commonly believed that they have flow independent features. This assumption of universal small scale structures is utilised in turbulence modelling. It is the subjective of this paper to discuss to what degree such a universal behaviour is present. Therefore, we performed a comprehensive investigation based on 2-point statistics (i.e. structure functions), multi-scale statistics (i.e. Markov analysis), and the analogue thermodynamic process (i.e. integral fluctuation theorem, IFT), as well as a multitude of 61 different turbulent flows with various kinds of turbulence generation.

Our first analysis step of the extensive dataset confirms the common 2-point statistics' scaling picture of homogeneous isotropic turbulence, cf. Kolmogorov (1962), figure 1. Furthermore, a closer investigation of local scaling exponents of structure functions and its features is also set in a universal dependence on Re_λ , which is supported by results of Mydlarski & Warhaft (1996), figure 2. The shown results do not allow a distinction between the different turbulent flows and no significant clustering with regard to the generation of turbulence could be detected. These results and their scattering are in agreement with other studies, e.g. Gylfason & Warhaft (2004), and confirm the common picture of universal small scale turbulence.

For this traditional scaling analysis of structure functions, we introduced two new quantities, Θ and σ_Θ , for the purpose of normalisation of scale and magnitudes of structure functions as in eq. (3.7). As these quantities are dimensional and contain information on large scale structures, we achieved a comparable basis and a collapse of the data of all considered turbulent flows.

After we have put our results in the context of the common understanding of turbulence, we continued with an advanced study which includes joint multi-scale statistics and the utilisation of the IFT as a consequence of the interpretation of the turbulent cascade as a non-equilibrium thermodynamic process.

As a first main result, we were able to show the validity of the IFT for all datasets, eq. (3.23) and figure 7. The high quality of the validity of the IFT leads us to propose that the IFT can be taken as a new general law for the turbulent cascade. Furthermore, utilising the IFT in combination with a self consistent optimisation procedure, we were able to work out the significant functional contributions to the stochastic cascade process, see eqs. (3.15) and (3.16), and figure 10. For all data, we see that these contributions are given by three aspects and parameters:

A deterministic part, expressed by $d_{11}(r)$ in eq. (4.7), corresponds to a returning force which pulls increments to the equilibrium state $u = 0$ while the cascade proceeds towards smaller scales. Thus, the deterministic part describes the reduction of the magnitude of the increments u_r with decreasing scales and fixes the average tendency of the cascade. The functional form of d_{11} in scale follows a power law, where the scaling exponent indicates, compared to the K62 model eq. (3.5), a decelerated decay of turbulent structures towards smaller scales.

Stochastic forces are represented by an additive and a multiplicative noise term, given by $d_{20}(r)$ and $d_{22}(r)$ in eqs. (4.8) and (4.9) respectively. Both stochastic forces add fluctuations to the deterministic evolution of increments and counteract the equilibrium tendency of the deterministic part. However, both are quite different in their significance and nature. The additive noise term d_{20} adds background fluctuations independent from u_r with a noticeable decrease with decreasing scale. In contrast, the multiplicative noise term d_{22} incorporates the energetic term u^2 as a source of fluctuations, just as the thermal energy of a reservoir is a source of fluctuations in a thermodynamic process. As d_{22} increases with decreasing scale, heavy tails of PDFs grow and extreme events get more likely towards smaller scales. This result is in agreement with the evolution of the energy transfer rate along the cascade, which starts off with a non-fluctuating average large value and becomes more and more fluctuating towards smaller scales. The *increasing* occurrence of extreme events is responsible for the phenomenon of small scale intermittency, and it is important to note that these fluctuations do not occur haphazardly but are well balanced with average realisations of the cascade process as checked by the IFT.

Our analysis demonstrated in particular that these three contributions are sufficient to also reproduce the measured evolution of skewness along the cascade in compliance with the four-fifth law, cf. figure 6. In other words, due to the absence of a term d_{21} , the two stochastic forces do not need to be correlated for the correct inclusion of skewness, contrary to many other stochastic models. Instead, with the additive noise acting predominantly on large scales and the multiplicative noise on small scales, an intuitive fluid dynamic picture of the turbulent cascade is conveyed: The additive noise injects energy on large scales, the linear drift is responsible for the transfer down the cascade, and the multiplicative noise effectively damps the fluctuations (weak noise for small u), superimposed by intermittent outbursts (strong noise for large u). In that picture, it is the linear drift term d_{11} that is responsible for the correct evolution of initial large scale skewness along the cascade.

The second main result is the reduction of the stochastic model to these three influences and their interpretation. Adding to that, the derived stochastic cascade model (based on the three parameters) leads to a closed set of differential equations for structure functions, eq. (4.6), which allows a decent reproduction of structure functions, and includes correct deviations from usual scaling behaviour, e.g. (Kolmogorov 1962).

Owing to our finding that the stochastic cascade process of turbulence can be represented by scale dependent parameters d_{ij} , we were able to investigate the aspects of universality in detail, figures 11 and 12. We found that the evolution in scale of d_{11} as well as d_{20} are universal in the sense that they are flow independent. Thus, their functional forms can be expressed by scale- and/or Re_λ -dependencies.

Our third main result is that in strong contrast to the findings of structure functions and parameters d_{11} and d_{20} , the parameter d_{22} as function of Re_λ splits up into distinct clusters for every considered dataset subgroup, which are characterised by specific large scale flow structures and the turbulence generation mechanism. Thus, we conclude that specific turbulent flows have their own particular multi-scale cascade, with other words,

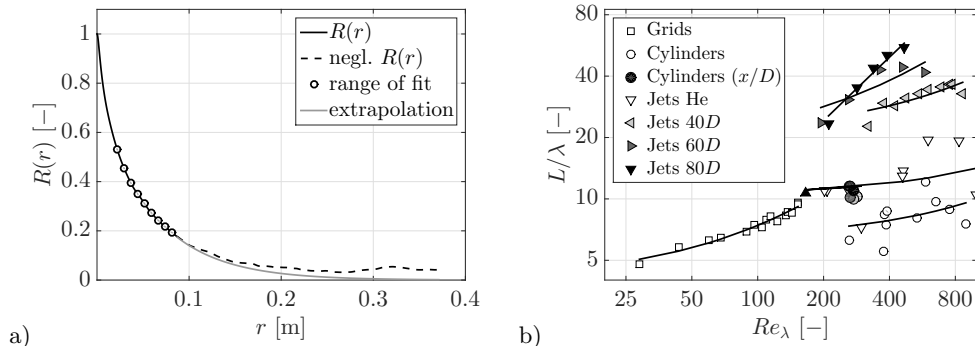


FIGURE 13. a) Illustration of the procedure of determining the integral length. Shown is the autocorrelation function, the considered part, solid black line and the neglected part, dashed black line, the range of fit, open circles and the extrapolation of $R(r)$, grey solid line. b) The length of the inertial range $\frac{L}{\lambda}$ as function of Re_λ for all datasets.

their own stochastic fingerprint.

We like to acknowledge the funding from DFG and the cooperations as well as discussions with D. Bastine, A. Engel, A. Fuchs, A. Hadjihosseini, P. Lind, P. Milan, R. Stresing, M. R. R. Tabar and M. Wächter as well as for the experimental datasets provided by O. Chanal, St. Lück and Ch. Renner.

6. Appendix

A1: Determination of integral length

The determination of the integral length is based on the definition in Batchelor (1953, p. 47), where the autocorrelation $R(r)$ is integrated from zero to infinity. From a particle point of view the integration is stopped before infinity, thus, an upper limit r_{up} is needed. For our data we investigate, going from zero to larger scales, if the autocorrelation decreases monotonically with $\partial_r R(r) \leq 0$ and $\partial_{rr} R(r) \geq 0$. For this case, the integration is done up to $R(r) \leq 0.01$. If this is not the case, a r_{up} is defined at the location where the monotonous decrease is violated. After $r = r_{up}$, the autocorrelation function becomes extrapolated as inspired by Batchelor (1953, pp. 92-96, fig. 5.2),

$$L = \int_0^{r_{up}} R(r) dr + \frac{e^{a \cdot r_{up} + b}}{a}. \quad (6.1)$$

The parameters a and b are obtained by a fit routine. The fitting range is between r_{low} and r_{up} . Low border r_{low} is chosen as the larger value of $R(r_{low}) = \frac{2}{e}$ or $3R(r_{up})$. Figure 13 a) exemplarily illustrates this procedure. Figure 13 b) shows the integral length L in units of the Taylor microscale λ versus the Taylor based Reynolds number. For all subgroups of datasets, the ratio $\frac{L}{\lambda}$ increases with Re_λ , as highlighted by linear fits. $\frac{L}{\lambda} \propto Re_\lambda$ can be derived from $L \approx \text{constant}$, $\lambda \propto Re^{-\frac{1}{2}}$ and $Re_\lambda \propto Re^{\frac{1}{2}}$ cf. Lück *et al.* (2006). Note, in figure 13 b) a double-logarithmic presentation is used for reasons of clarity.

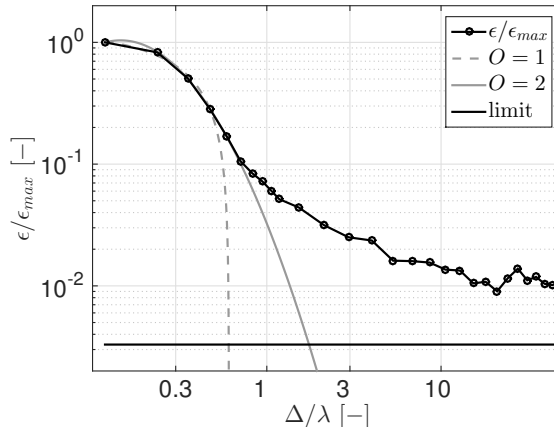


FIGURE 14. Test of the Markov property by normalised ϵ , according to eq. (3.18), with PDFs from the left and right hand side of eq. (6.2). The limit indicates the best expected ϵ . Fits of first and second order estimates l_{EM} .

A2: Einstein-Markov coherence length

The Einstein-Markov coherence length l_{EM} is a length at which

$$p(u_r|u_{r+l_\Delta}) = p(u_r|u_{r+l_\Delta}, u_{r+2l_\Delta} = 0 \pm \chi), \quad (6.2)$$

$$\chi = 0.1\sigma_v \quad (6.3)$$

is fulfilled. Lück *et al.* (2006) used the Wilcoxon test to verify this length, which can be considered as a *linear measure*. Here a test is used which is based on eq. (3.18). Since eq. (3.18) is a logarithmic measure, rare events are more strongly weighted. Figure 14 shows an exemplary examination of eq. (6.2) under variation of Δ , which is given in units of λ . The first steep part of ϵ is extrapolate to estimate l_{EM} . A first order polynomial ($O = 1$) leads to a similar result as published by Lück *et al.* (2006) and a second order polynomial ($O = 2$) leads to a higher estimation of $l_{EM} \approx 2\lambda$. For both estimations ($O = 1$ and $O = 2$) of l_{EM} a non-Markovian share remain. Note, the relation between l_{EM} and λ slightly changes the IFT convergence, $l_{EM} = \lambda \rightarrow \langle I_{max} \rangle \approx 1.02$ and $l_{EM} = 2\lambda \rightarrow \langle I_{max} \rangle \approx 1.01$.

A3: Characterisation of norms

Figure 15 shows the dimensional norms Θ and σ_Θ as function of Re_λ . Θ is plotted in a double-logarithmic fashion, thereby a power law dependence from Re_λ becomes evident. σ_Θ depends linearly on Re_λ , figure 15 b). For both quantities the different generated flows show up in individual clusters, which are, interestingly, arranged in different ways. Although, Θ and σ_Θ are connected by their definition, the different arrangement and the different functional dependence on Re_λ show that they are not trivially linked to each other. The ratio $\frac{\Theta}{\lambda}$ (e.g. as function of Re_λ) shows a rather scattered distribution, values are between 2 and ~ 4 , however, some ratios go up to ~ 7 .

A4: Structure functions deduced by $D^{(1,2)}$

Eq. (4.6) allows to calculate the structure functions and $\xi_\kappa(r)$ from the parameters d_{ij} . Figure 16 shows our approaches of proper parametrisations according to $d_{11} = (\alpha_{11} \frac{r}{l_{EM}} + \beta_{11})^{-\frac{1}{2}}$, $d_{22} = \alpha_{22} \ln(\frac{r}{l_{EM}}) + \beta_{22}$ and $d_{20} = (\alpha_{20} \ln(\frac{r}{l_{EM}}) + \beta_{20})^{\frac{1}{3}}$. For this illustration

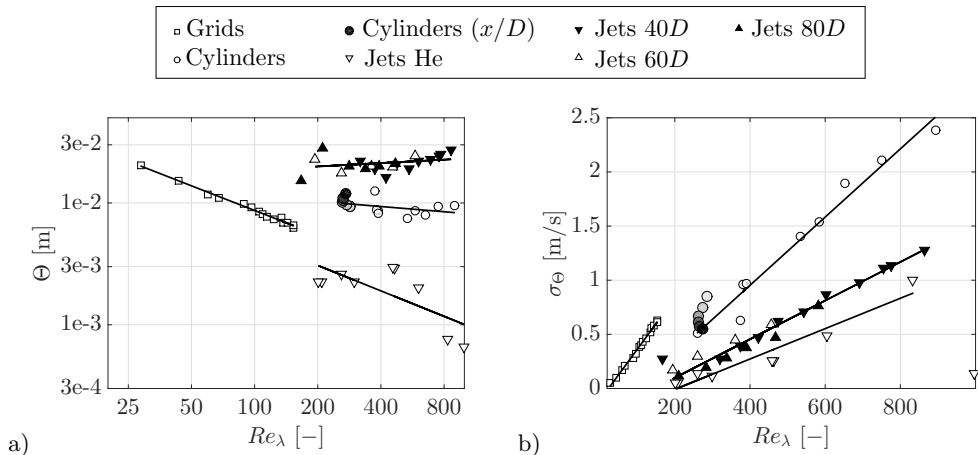


FIGURE 15. a) shows the norm Θ versus Re_λ in a double-logarithmic plot. b) shows the norm σ_Θ versus Re_λ . Both norms are shown for all datasets. Trends are highlighted by linear fit functions.

Type	$ Re_\lambda $	α_{11}	β_{11}	$100\alpha_{22}$	$100\beta_{22}$	$100\alpha_{20}$	$100\beta_{20}$
grid	28	3.85	-0.29	-0.47	0.93	2.19	1.15
grid (i)	153	3.97	-0.29	-0.56	1.68	2.27	1.34
free jet (i)	166	4.19	-0.91	-0.85	2.2	2.16	0.98

TABLE 3. d_{ij} parametrisation in terms of α_{ij} and β_{ij} , see also table 1.

three different datasets are used. The Re_λ -values and the corresponding fit parameters α_{ij} and β_{ij} as well as the flow type are summarised in table 3.

The local scaling exponents are shown in figure 17, which are deduced directly from the velocity increments and from the parameters using eq. (4.6). The values of the optimised $D^{(1,2)}$ as well as the mentioned fit functions of parameters d_{ij} are used. Here - as an exception - with $l_{EM} = \lambda$ to highlight the crossing of K62. Note, the *jumpy development of ξ_κ* is caused by a linear interpolation of $D^{(1,2)}$. An error margin $\Delta\xi_\kappa(r)$ of $\xi_\kappa(r)$ is derived from the experimental data. This is done by splitting the measured data in n -groups and determining n -time $\xi_\kappa(r)$, from which the standard deviation $\sigma(\xi_\kappa^n(r))$ is calculated. In this way ($n = 50$)

$$\Delta\xi_\kappa(r) = \frac{\sigma(\xi_\kappa^n(r))}{\sqrt{n}} \quad (6.4)$$

is determined. As an orientation also Kolmogorov's prediction according to eq. (3.5) is shown, labelled K62, likewise to figure 2 a).

A5: Interpretation of $D^{(1)}$ and $D^{(2)}$ with the short time propagator

The interpretation of $D^{(1,2)}$ and d_{11} , d_{22} , d_{20} is done by modifying optimised $D^{(1,2)}$ and presenting the corresponding short time propagator. The short time propagator deduced by unmodified d_{11} , d_{22} and d_{20} (regular optimised) is shown in figure 18 a). The agreement is good between short time propagator and the experimental reference data. In figure 18 b) d_{11} is multiplied by 5, whereas d_{22} and d_{20} are unmodified. This multiplication twists the diagonal of short time propagator in comparison to the experimental reference

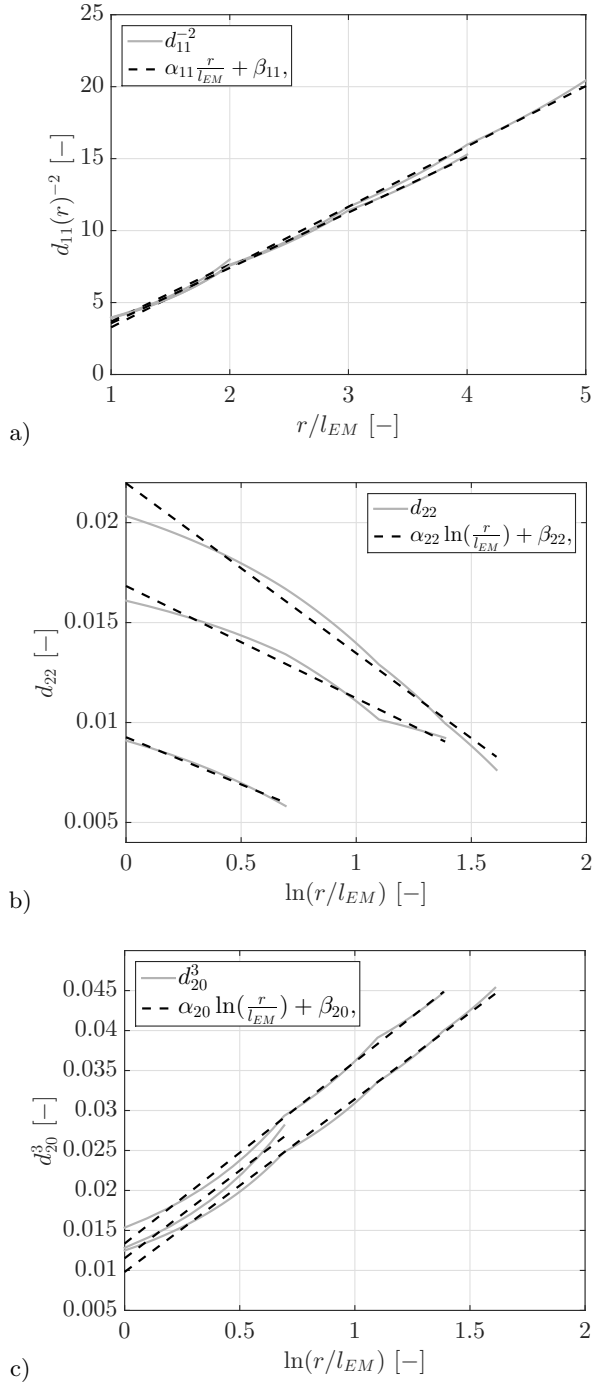


FIGURE 16. d_{ij} in a linearised form as well as fit functions. Length of d_{ij} corresponds to Re_λ , see table 3.

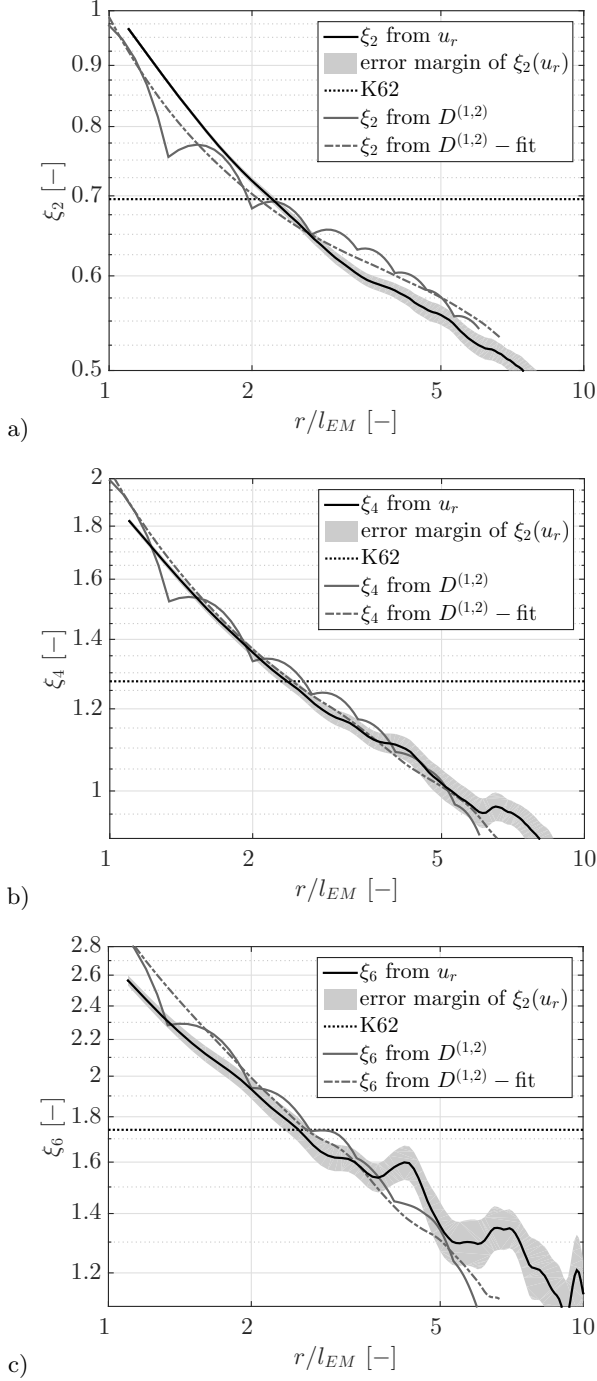


FIGURE 17. Local scaling exponent $\xi_\kappa(r)$ deduced from experimental data, reconstructed by $D^{(1,2)}$ as well as their fits. Also Kolmogorov's prediction is shown (K62) and an error margin of the experimental data. Grid (i) is used as exemplary dataset, characterised in table 1 and 3.

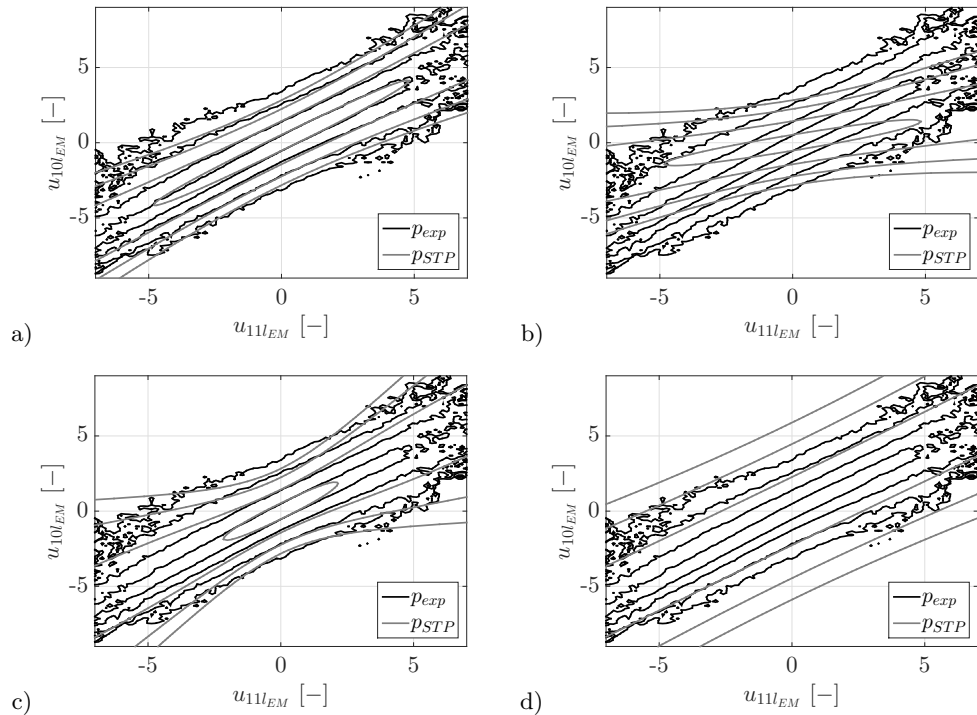


FIGURE 18. One exemplary experimentally found conditional PDF, p_{exp} (black) (subgroup (v), $Re_\lambda = 475$) and four different results of the short time propagator p_{STP} (grey). Figure a) shows the short time propagator regarding to optimised $D^{(1,2)}$. In figure b) the same is shown as in a) except that d_{11} is multiplied by 5. In figure c) only d_{22} is multiplied by 5 and in figure d) only d_{20} is multiplied by 5.

data. Thus, we see that the magnitude of d_{11} controls the diagonal. In figure 18 c) d_{22} is multiplied by 5, whereas d_{11} and d_{20} are unmodified. An enlarged d_{22} increases the curvature of the isolines in the contour plot. Therefore, the probability for extreme events increases, which is equivalent to an increased intermittency and to more fat tailed unconditional PDFs. In figure 18 d) d_{20} is multiplied by 5, whereas d_{11} and d_{22} are unmodified. Here the reconstructed distribution gets broader around the distribution diagonal.

A6: Single developments of d_{11} , d_{22} and d_{20} in scale

For the sake of completeness, the coefficients d_{11} , d_{22} and d_{20} are shown for cylinder and free jet flows as function of scale in figures 19 - 21. These figures are just the same as figure 10.

A7: d_{22} as function of $\frac{L}{\lambda}$

Findings of figures 12 e) and f) can be further investigated in terms of universality by interpreting d_{22} as function of a different quantity. For instance, plotting d_{22} as function of the dimensionless length $\frac{L}{\lambda}$, which is the relative length of the inertial range. The results become newly sorted and give a much more uniform picture, see figures 22 a) and b). Although, single free jet subgroups might be systematically distinguished in terms of the relative distance to the nozzle, the entire free jet datasets show a rather uniform group in contrast to figures 12 e) and f). The relative location of the *Cylinder* subgroup

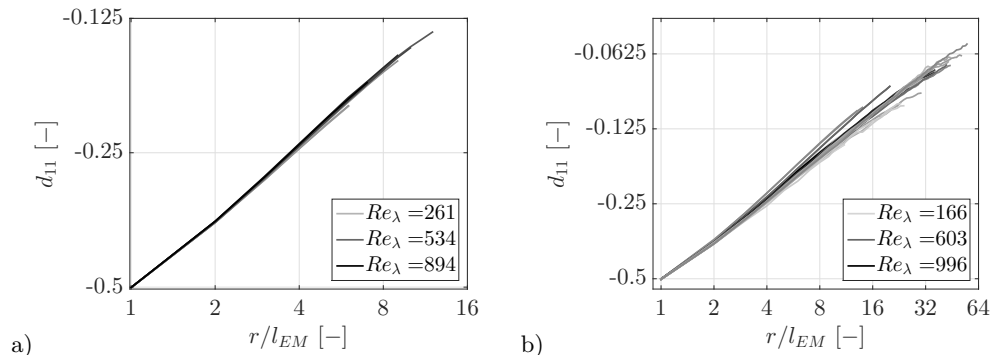


FIGURE 19. d_{11} as function of scale, of cylinder flows (a) and free jet flows (b). Lines' greyscale indicates Re_λ .

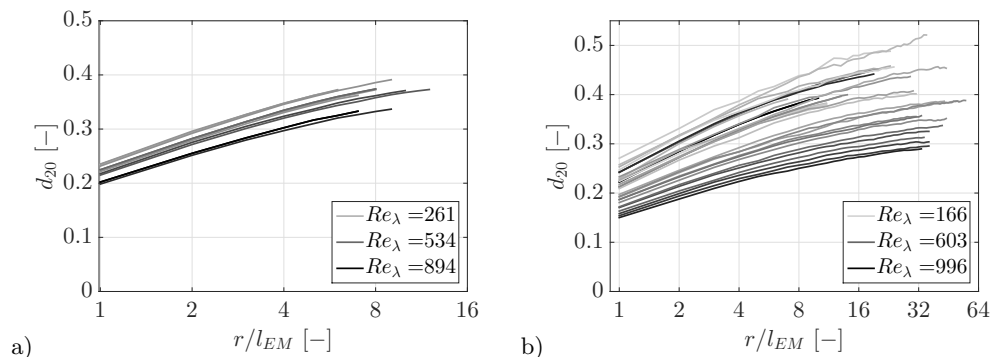


FIGURE 20. d_{20} as function of scale, of cylinder flows (a) and free jet flows (b). Lines' greyscale indicates Re_λ .

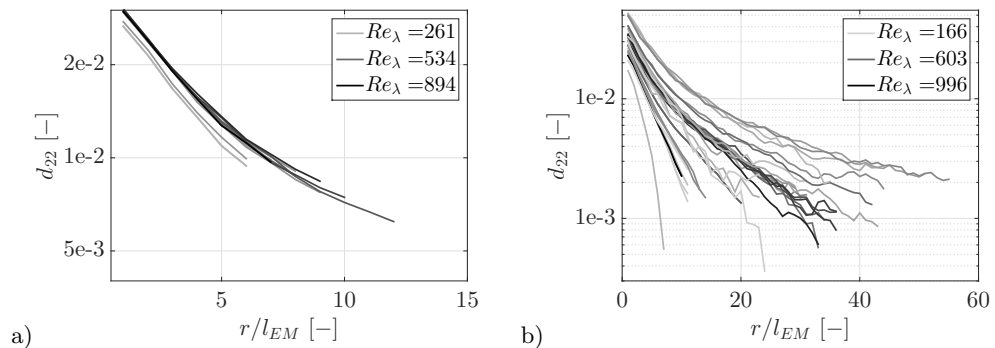


FIGURE 21. d_{22} as function of scale, of cylinder flows (a) and free jet flows (b). Lines' greyscale indicates Re_λ .

differs clearly from the other data in this presentation. Although d_{22} is more sorted, we come to the same conclusion as above, intermittency features in terms of d_{22} are non-universal, and single flow types become apparent.

REFERENCES

ARNEODO, A., BAUDET, C., BELIN, F., BENZI, R., CASTAING, B., CHABAUD, B., CHAVARRIA,

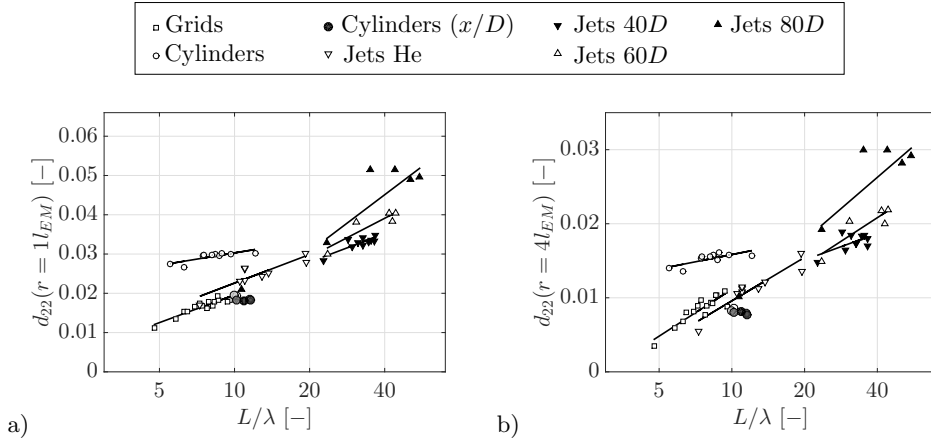


FIGURE 22. Parameter d_{22} as function of L/λ at two fixed scales ($r = l_{EM}$ and $4l_{EM}$). Additionally, *linear* fit functions indicate trends. Plots are semi-logarithmically plotted.

- R., CILIBERTO, S., CAMUSSI, R., CHILLÁ, F., DUBRULLE, B., GAGNE, Y., HEBRAL, B., HERWEIJER, J., MARCHAND, M., MAURER, J., MUZY, J. F., NAERT, A., NOULLEZ, A., PEINKE, J., ROUX, F., TABELING, P., VAN DE WATER, W. & WILLAIME, H. 1996 Structure functions in turbulence, in various flow configurations, at reynolds number between 30 and 5000, using extended self-similarity. *EPL (Europhysics Letters)* **34** (6), 411.
- ARNEODO, A., MUZY, J.F. & ROUX, S.G. 1997 Experimental analysis of self-similarity and random cascade process: Application to fully developed turbulence data. *J. Phys. II France* **7**, 363 – 370.
- ARONSON, D. & LÖFDAHL, L. 1993 The plane wake of a cylinder: Measurements and inferences on turbulence modeling. *Physics of Fluids A* **5**, 1433–1437.
- BATCHELOR, G. K. 1953 *The theory of homogeneous turbulence*. Cambridge: Cambridge science classic.
- BENZI, R., BIFERALE, L., CILIBERTO, S., STRUGLIA, M.V. & TRIPICCIONE, R. 1996 Generalized scaling in fully developed turbulence. *Physica D: Nonlinear Phenomena* **96** (1–4), 162–181.
- BENZI, R., CILIBERTO, S., TRIPICCIONE, R., BAUDET, C., MASSAIOLI, F. & SUCCI, S. 1993 Extended self-similarity in turbulent flows. *Phys. Rev. E* **48**, R29–R32.
- CASTAING, B. & DUBRULLE, B. 1995 Fully developed turbulence: A unifying point of view. *J. Phys. II France* **5**, 895 –899.
- CHANAL, O., CHABAUD, B., CASTAING, B. & HÉBRAL, B. 2000 Intermittency in a turbulent low temperature gaseous helium jet. *The European Physical Journal B - Condensed Matter and Complex Systems* **17** (2), 309–317.
- CLAY 2000 *Millennium problems*. Clay Mathematics Institute: <http://www.claymath.org/millennium-problems>.
- DAVIDSON, P. A. 2004 *Turbulence: an introduction for scientists and engineers*. Oxford University Press, USA.
- DAVOUDI, JAHANSHAH & TABAR, M. REZA RAHIMI 2000 Multiscale correlation functions in strong turbulence. *Physical Review E* **61** (6).
- DUBRULLE, B. 2000 Finite size scale invariance. *Eur. Phys. J. B* **14**, 757771.
- EINSTEIN, A. 1905 Über die von der molekularkinetischen theorie der wärme geforderte bewegung von in ruhenden flüssigkeiten suspendierten teilchen. *Annalen der Physik* **322** (8), 549–560.
- FELLER, WILLIAM 1968 *An Introduction to Probability Theory and Its Applications*, , vol. 1. Wiley.
- FRIEDRICH, R. & PEINKE, J. 1997a Description of a turbulent cascade by a fokker-planck equation. *Phys. Rev. Lett.* **78**, 863.

- FRIEDRICH, R. & PEINKE, J. 1997*b* Statistical properties of a turbulent cascade. *Physica D* **102**, 147.
- FRIEDRICH, R. & PEINKE, J. 2009 Fluid dynamics, turbulence. In *Encyclopedia of Complexity and Systems Science* (ed. Robert A. Meyers), pp. 3642 – 3661. New York, NY: Springer.
- FRIEDRICH, R., PEINKE, J. & NAERT, A. 1997 A new approach to characterize disordered structures. *Z. Naturforsch* **52 a**, 588 – 592.
- FRIEDRICH, R., PEINKE, J., SAHIMI, M. & TABAR, M. REZA RAHIMI 2011 Approaching complexity by stochastic processes: From biological systems to turbulence. *Phys. Report* **506**, 87–162.
- FRISCH, U. 2001 *Turbulence: the legacy of A. N. Kolmogorov*. Cambridge University Press.
- GAGNE, YVES, MARCHAND, MURIEL & CASTAING, BERNARD 1994 Conditional velocity pdf in 3-D turbulence. *Journal de Physique II* **4** (1), 1–8.
- GLEDZER, E. 1997 On the Taylor hypothesis corrections for measured energy spectra of turbulence. *Physica D Nonlinear Phenomena* **104**, 163–183.
- GOTTSCHALL, JULIA & PEINKE, JOACHIM 2008 On the definition and handling of different drift and diffusion estimates. *New Journal of Physics* **10** (8), 083034.
- GRAUER, RAINER, HOMANN, HOLGER & PINTON, JEAN-FRANCOIS 2012 Longitudinal and transverse structure functions in high-reynolds-number turbulence. *New Journal of Physics* **14** (6), 063016.
- GYLFASON, A. & WARHAFT, Z. 2004 On higher order passive scalar structure functions in grid turbulence. *Physics of Fluids* **16**, 4012–4019.
- HONISCH, CHRISTOPH & FRIEDRICH, RUDOLF 2011 Estimation of kramers-moyal coefficients at low sampling rates. *Phys. Rev. E* **83**, 066701.
- HURST, D. & VASSILICOS, J. C. 2007 Scalings and decay of fractal-generated turbulence. *Physics of Fluids* **19** (3).
- KEYLOCK, C. J., STRESING, R. & PEINKE, J. 2015 Gradual wavelet reconstruction of the velocity increments for turbulent wakes. *Physics of Fluids* **27** (2).
- KLEINHANS, D., FRIEDRICH, R., NAWROTH, A. P. & PEINKE, J. 2005 An iterative procedure for the estimation of drift and diffusion coefficients of langevin processes. *Phys. Letters A* **346**, 42–46.
- KOLMOGOROV, A. N. 1941 Dissipation of energy in locally isotropic turbulence. *Dokl. Akad. SSSR* **32**, 16–18.
- KOLMOGOROV, A. N. 1962 A refinement of previous hypotheses concerning the local structure of turbulence in a viscous incompressible fluid at high reynolds number. *Journal of Fluid Mechanics* **13**, 82–85.
- KUCZAJ, ARKADIUSZ K., GEURTS, BERNARD J. & MCCOMB, W. DAVID 2006 Nonlocal modulation of the energy cascade in broadband-forced turbulence. *Phys. Rev. E* **74**, 016306.
- LAVAL, J-P., DUBRULLE, B. & NAZARENKO, S. 2001 Nonlocality and intermittency in three-dimensional turbulence. *Physics of Fluids* **13**, 1995.
- LEMONS, DON S. 1997 Paul Langevin's 1908 paper "On the Theory of Brownian Motion" ["Sur la théorie du mouvement brownien," C. R. Acad. Sci. (Paris) 146, 530-533 (1908)]. *American Journal of Physics* **65** (11), 1079.
- LIN, C. C. 1950 On taylor's hypothesis in wind tunnel turbulence. *Memor. U.S. Naval Ord. Lab. no. 10775* .
- LÜCK, ST., RENNER, CH., PEINKE, J. & FRIEDRICH, R. 2006 The markov-einstein coherence length - a new meaning for the taylor length in turbulence. *Physics Letters A* **359** (5), 335–338.
- LUMLEY, J. L. 1965 Interpretation of time spectra measured in highintensity shear flows. *Physics of Fluids* **8** (6), 1056–1062.
- LUNDGREN, T. S. 1967 Distribution functions in the statistical theory of turbulence. *Physics of Fluids* **10** (5), 969–975.
- L'VOV, VICTOR & PROCACCIA, ITAMAR 1996 Fusion rules in turbulent systems with flux equilibrium. *Phys. Rev. Lett.* **76**, 2898–2901.
- MARCQ, PHILIPPE & NAERT, ANTOINE 2001 A langevin equation for turbulent velocity increments. *Physics of Fluids* **13**, 2590 – 2595.
- MELIUS, MATTHEW S., TUTKUN, MURAT & CAL, RAÚL BAYOÁN 2014 Identification of markov

- process within a wind turbine array boundary layer. *Journal of Renewable and Sustainable Energy* **6** (2).
- MONIN, A.S. 1967 Equations of turbulent motion. *Journal of Applied Mathematics and Mechanics* **31** (6), 1057 – 1068.
- MONIN, ANDRE SERGEEVICH, IAGLOM, AM & LUMLEY, JOHN LEASK 2007 *Statistical fluid mechanics: mechanics of turbulence*, , vol. 1. Courier Corporation.
- MURZYN, FRÉDÉRIC & BÉLORGEY, MICHEL 2005 Experimental investigation of the grid-generated turbulence features in a free surface flow. *Experimental Thermal and Fluid Science* **29** (8), 925 – 935.
- MYDLARSKI, L. & WARHAFT, Z. 1996 On the onset of high-reynolds-number grid-generated wind tunnel turbulence. *Journal of Fluid Mechanics* **320**, 331–368.
- NAERT, A., FRIEDRICH, R. & PEINKE, J. 1997 Fokker-Planck equation for the energy cascade in turbulence. *Physical Review E* **56** (6), 6719–6722.
- NAGATA, KOUJI, SAKAI, YASUHIKO, INABA, TAKUTO, SUZUKI, HIROKI, TERASHIMA, OSAMU & SUZUKI, HIROYUKI 2013 Turbulence structure and turbulence kinetic energy transport in multiscale/fractal-generated turbulence. *Physics of Fluids* **25** (6).
- NAWROTH, A. P., PEINKE, J., KLEINHANS, D. & FRIEDRICH, R. 2007 Improved estimation of fokker-planck equations through optimisation. *Phys. Rev. E* **76** (056102).
- NELKIN, M. 1992 In What Sense Is Turbulence an Unsolved Problem? *Science* .
- NICKELSEN, DANIEL 2017 Master equation for She-Leveque scaling and its classification in terms of other Markov models of developed turbulence. *Journal of Statistical Mechanics: Theory and Experiment* **2017** (7), 073209.
- NICKELSEN, DANIEL & ENGEL, ANDREAS 2013 Probing small-scale intermittency with a fluctuation theorem. *Physical Review Letters* **110**, 214501.
- NOVIKOV, E.A. 1994 Infinitely divisible distributions in turbulence. *Phy. Rev. E (R)* **50**, R3303–R3305.
- PINTON, J. F. & LABBÉ, R. 1994 Correction to the taylor hypothesis in swirling flows. *J. Phys. II France* **4** (9), 1461–1468.
- POPE, S. B. 2000 *Turbulent Flows*. Cambridge University Press.
- R. FRIEDRICH, J. ZELLER & PEINKE, J. 1998 A note on three-point statistics of velocity increments in turbulence. *Europhys. Lett.* **41** (2).
- REINKE, N., FUCHS, A., HÖLLING, M. & PEINKE, J. 2014 Stochastic analysis of a fractal grid wake. *Progress in Turbulence VI, Proceedings of the iTi Conference on Turbulence 2014, Springer Proceedings in Physics* **6**.
- REINKE, N., NICKELSEN, D., ENGEL, A. & PEINKE, J. 2016 Application of an integral fluctuation theorem to turbulent flows. *Progress in Turbulence VI, Proceedings of the iTi Conference on Turbulence 2014, Springer Proceedings in Physics* **165**, 19 – 25.
- RENNER, C. 2002 Markowanalysen stochastisch fluktuiender zeitserien. *Dissertation* .
- RENNER, C., PEINKE, J. & FRIEDRICH, R. 2001 Experimental indications for markov properties of small-scale turbulence. *J. Fluid Mech.* **433**, 383–409.
- RENNER, CH., PEINKE, J. & FRIEDRICH, R. 2002a On the interaction between velocity increment and energy dissipation in the turbulent cascade. *arXiv* p. 18, arXiv: 0211121.
- RENNER, C., PEINKE, J., FRIEDRICH, R., CHANAL, O. & CHABAUD, B. 2002b Universality of small scale turbulence. *Phys. Rev. Lett.* **89**, 124502.
- RISKEN, H. 1984 *The Fokker-Planck Equation*. Heidelberg: Springer.
- SEIFERT, U. 2005 Entropy Production along a Stochastic Trajectory and an Integral Fluctuation Theorem. *Physical Review Letters* **95** (4), 040602, arXiv: cond-mat/0503686.
- SEIFERT, UDO 2012 Stochastic thermodynamics, fluctuation theorems and molecular machines. *Reports on Progress in Physics* **75** (12), 126001.
- SEKIMOTO, KEN 1998 Langevin Equation and Thermodynamics. *Progress of Theoretical Physics Supplement* **130**, 17–27.
- SHE, ZHEN-SU & WAYMIRE, EDWARD C. 1995 Quantized energy cascade and log-poisson statistics in fully developed turbulence. *Phys. Rev. Lett.* **94**, 262 –899.
- SIEFERT, M. & PEINKE, J. 2004 Different cascade speeds for longitudinal and transverse velocity increments of small-scale turbulence. *Physical Review E* **70** (015302(R)).
- SIEFERT, M. & PEINKE, J. 2006 Joint multi-scale statistics of longitudinal and transversal increments in small-scale wake turbulence. *Journal of Turbulence* **7**, N50.

- SINHUBER, M. 2015 On the scales of turbulent motion at high reynolds numbers. *Dissertation* .
- SINHUBER, M., G.O., BEWLEY & E., BODENSCHATZ 2017 Dissipative effects on inertial-range statistics at high reynolds numbers. *Phys. Rev. Lett.* **119**, 134502.
- STRESING, R., KLEINHANS, D., FRIEDRICH, R. & PEINKE, J. 2012 Publisher's note: Different methods to estimate the einstein-markov coherence length in turbulence [phys. rev. e **83**, 046319 (2011)]. *Phys. Rev. E* **85**, 029907.
- STRESING, R. & PEINKE, J. 2010 Towards a stochastic multi-point description of turbulence. *New Journal of Physics* **12** (10), 103046.
- STRESING, R., PEINKE, J., SEUD, R. E. & VASSILICOS, J. C. 2010 Defining a new class of turbulent flows. *Phys. Rev. Lett.* **104**, 194501.
- TAYLOR, G. I. 1938 The spectrum of turbulence. *Proceedings of the Royal Society of London A: Mathematical, Physical and Engineering Sciences* **164** (919), 476–490.
- TONG, CHENNING & WARHAFT, Z. 1995 Passive scalar dispersion and mixing in a turbulent jet. *Journal of Fluid Mechanics* **292**, 1–38.
- TUTKUN, M. & MYDLARSKI, L. 2004 Markovian properties of passive scalar increments in grid-generated turbulence. *New Journal of Physics* **6** (1), 49.
- VALENTE, P. C. & VASSILICOS, J. C. 2012 Universal dissipation scaling for nonequilibrium turbulence. *Phys. Rev. Lett.* **108**, 214503.